Meningioma DNA methylation groups identify biological drivers and therapeutic vulnerabilities

Abrar Choudhury [1,2,3,4], Stephen T. Magill [5,18 ✉], Charlotte D. Eaton[1,2,18], Briana C. Prager[6], William C. Chen[1,2], Martha A. Cady[1,2], Kyounghee Seo[1,2], Calixto-Hope G. Lucas [1,2,7], Tim J. Casey-Clyde [1,2], Harish N. Vasudevan[1,2], S. John Liu [1,2], Javier E. Villanueva-Meyer[2,8], Tai-Chung Lam[9], Jenny Kan-Suen Pu[10], Lai-Fung Li [10], Gilberto Ka-Kit Leung[10], Danielle L. Swaney [11,12,13], Michael Y. Zhang[1,2], Jason W. Chan[1], Zhixin Qiu [6], Michael V. Martin[2], Matthew S. Susko[1], Steve E. Braunstein[1], Nancy Ann Oberheim Bush[2,14], Jessica D. Schulte[15], Nicholas Butowski[2], Penny K. Sneed[1], Mitchel S. Berger[2], Nevan J. Krogan [11,12,13], Arie Perry [2,7], Joanna J. Phillips [2,7], David A. Solomon [7], Joseph F. Costello [2], Michael W. McDermott[2,16], Jeremy N. Rich [17 ✉] and David R. Raleigh [1,2 ✉]

Meningiomas are the most common primary intracranial tumors. There are no effective medical therapies for meningioma patients, and new treatments have been encumbered by limited understanding of meningioma biology. Here, we use DNA methylation profiling on 565 meningiomas integrated with genetic, transcriptomic, biochemical, proteomic and single-cell approaches to show meningiomas are composed of three DNA methylation groups with distinct clinical outcomes, biological drivers and therapeutic vulnerabilities. Merlin-intact meningiomas (34%) have the best outcomes and are distinguished by *NF2*/Merlin regulation of susceptibility to cytotoxic therapy. Immune-enriched meningiomas (38%) have intermediate outcomes and are distinguished by immune infiltration, *HLA* expression and lymphatic vessels. Hypermitotic meningiomas (28%) have the worst outcomes and are distinguished by convergent genetic and epigenetic mechanisms driving the cell cycle and resistance to cytotoxic therapy. To translate these findings into clinical practice, we show cytostatic cell cycle inhibitors attenuate meningioma growth in cell culture, organoids, xenografts and patients.

DNA methylation profiling was performed on 565 meningiomas from patients with comprehensive clinical follow-up who were treated at two independent institutions from 1991 to 2019 (Supplementary Table 1). Consistent with typical meningioma outcomes, local freedom from recurrence (LFFR) and overall survival (OS) were worse with higher World Health Organization (WHO) grade, recurrent presentation or subtotal resection (Supplementary Fig. 1). Meningiomas were stratified into a 200-sample discovery cohort from the University of California, San Francisco (UCSF; median follow-up, 6.3 years) and a consecutive 365-sample validation cohort from The University of Hong Kong (median follow-up, 5.3 years) (Supplementary Table 1). Meningiomas have an abundance of genomic copy-number variants (CNVs)[1,2] (Fig. 1a), and standard bioinformatic approaches can report inaccurate β-methylation values at genomic loci with

CNVs[3]. We hypothesized that controlling for the influence of CNVs on β-methylation values, coupled with mechanistic and functional studies, may reveal insights into meningioma biology and inform new treatments for meningioma patients. Prior meningioma DNA methylation studies have not accounted for the influence of CNVs on β-methylation values and have reported variable groups of tumors[2,4–8], sometimes with overlapping clinical outcomes[4]. Thus, questions remain regarding the biological drivers and therapeutic vulnerabilities across meningioma DNA methylation groups.

The 565 meningioma DNA methylation profiles comprising the discovery or validation cohorts were analyzed using the SeSAMe preprocessing pipeline (Extended Data Fig. 1a–e), which controls for the influence of homozygous or heterozygous CNVs on β-methylation values[3]. *K*-means consensus clustering, continuous distribution functions and unsupervised hierarchical clustering

[1]Department of Radiation Oncology, University of California, San Francisco, San Francisco, CA, USA. [2]Department of Neurological Surgery, University of California, San Francisco, San Francisco, CA, USA. [3]Medical Scientist Training Program, University of California, San Francisco, San Francisco, CA, USA. [4]Biomedical Sciences Graduate Program, University of California, San Francisco, San Francisco, CA, USA. [5]Department of Neurological Surgery, Northwestern University, Chicago, IL, USA. [6]Department of Medicine, University of California, San Diego, San Diego, CA, USA. [7]Department of Pathology, University of California, San Francisco, San Francisco, CA, USA. [8]Department of Radiology and Biomedical Imaging, University of California, San Francisco, San Francisco, CA, USA. [9]Department of Clinical Oncology, The University of Hong Kong, Pokfulam, Hong Kong. [10]Division of Neurosurgery, Department of Surgery, The University of Hong Kong, Pokfulam, Hong Kong. [11]J. David Gladstone Institutes, California Institute for Quantitative Biosciences, San Francisco, CA, USA. [12]California Institute for Quantitative Biosciences, San Francisco, CA, USA. [13]Department of Cellular and Molecular Pharmacology, University of California, San Francisco, San Francisco, CA, USA. [14]Department of Neurology, University of California, San Francisco, San Francisco, CA, USA. [15]Department of Neurosciences, University of California, San Diego, San Diego, CA, USA. [16]Miami Neuroscience Institute, Baptist Health, Miami, FL, USA. [17]Department of Neurology, University of Pittsburgh, Pittsburgh, PA, USA. [18]These authors contributed equally: Stephen T. Magill, Charlotte D. Eaton. ✉e-mail: stephen.magill@northwestern.edu; drjeremyrich@gmail.com; david.raleigh@ucsf.edu
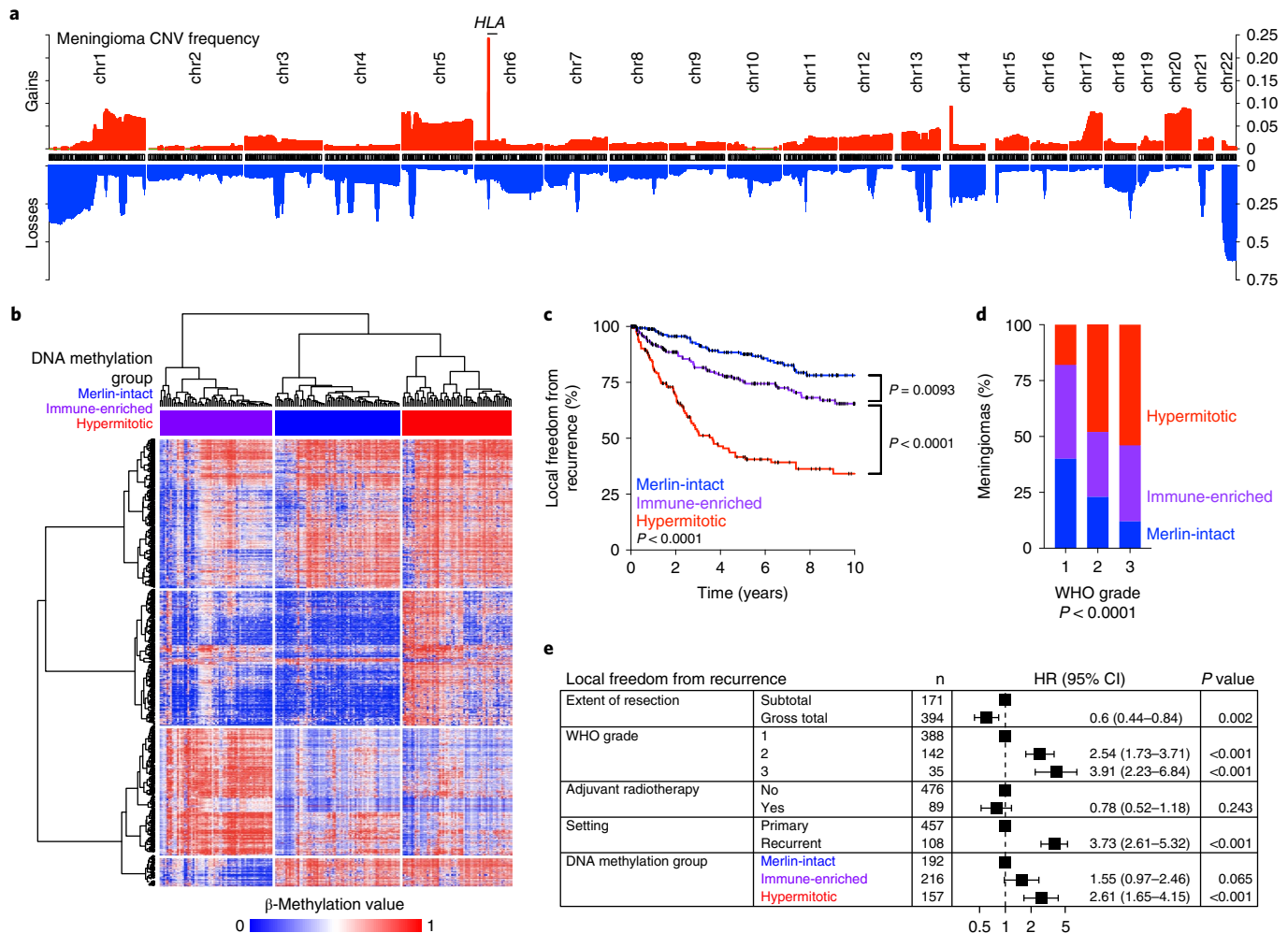
Fig. 1 | Meningiomas are composed of three DNA methylation groups with distinct outcomes. a, Frequency of copy-number losses (blue) or gains (red) across the discovery and validation cohorts (*n* = 565). **b**, Unsupervised hierarchical clustering of meningiomas from the discovery cohort (*n* = 200) using 2,000 differentially methylated DNA probes. **c**, Kaplan–Meier curves for meningioma LFFR from the discovery and validation cohorts (*n* = 565) across DNA methylation groups (log-rank test). **d**, Meningioma WHO grades (*n* = 565) across DNA methylation groups (chi-squared test, two sided). **e**, Multivariable regression hazard ratio (HR) forest plots for LFFR using meningioma clinical variables and DNA methylation groups (*n* = 565, Cox proportional hazards model, Wald test, two sided, no adjustment for multiple comparisons). Boxes represent means, and error bars represent 95% confidence intervals (CIs).

revealed three meningioma DNA methylation groups in the discovery cohort (Fig. 1b and Extended Data Fig. 1a–e), which was validated as the optimal number of groups in the validation cohort (Extended Data Fig. 2a). A multiclass support vector machine classifier with 97.9% accuracy (95% CI, 89.2%–99.9%; $P < 2.2 \times 10^{-16}$) was constructed to assign meningiomas from the validation cohort into DNA methylation groups (Extended Data Fig. 2b). Kaplan–Meier analyses showed DNA methylation groups were distinguished by differences in LFFR and OS (Fig. 1c and Supplementary Fig. 2a) and correlated with WHO grade, sex, prior radiotherapy and location (Fig. 1d and Supplementary Fig. 2b). DNA methylation groups were independently prognostic for LFFR on Kaplan–Meier analysis across WHO grades (Supplementary Fig. 2c,d) and on multivariable regression (Fig. 1e and Supplementary Fig. 2e).

Meningioma DNA methylation groups had different CNV landscapes in aggregate (Fig. 1a and Supplementary Fig. 3a,b), but individual CNVs or combinations of CNVs were insufficient to define all meningiomas in each DNA methylation group (Supplementary Fig. 3c). Reanalysis using the minfi preprocessing pipeline[9], which does not control for the influence of CNVs on β-methylation values,

reassigned 21% of meningiomas across an unclear optimal number of DNA methylation groups with overlapping clinical outcomes (Extended Data Fig. 3). Thus, controlling for the influence of CNVs on β-methylation values improves meningioma DNA methylation grouping and discrimination of clinical outcomes.

NF2/Merlin drives meningioma apoptosis

Meningiomas are common in patients with neurofibromatosis type 2, a complex autosomal syndrome caused by loss of *NF2* on chromosome 22q, which encodes the tumor suppressor protein Merlin[10]. *NF2* is also the most recurrently mutated gene in sporadic and radiation-induced meningiomas[11–15]. CNVs defined using DNA methylation profiles revealed chromosome 22q copy-number deletions of any size containing the entire *NF2* locus in 86% of syndromic (*n* = 18) or radiation-induced meningiomas (*n* = 34), which were predominantly found in DNA methylation groups with intermediate or poor clinical outcomes (96%). Only 17% of meningiomas in the DNA methylation group with the best outcomes had chromosome 22q copy-number deletions of any size containing the entire *NF2* locus (*n* = 32 of 192) compared to 76%
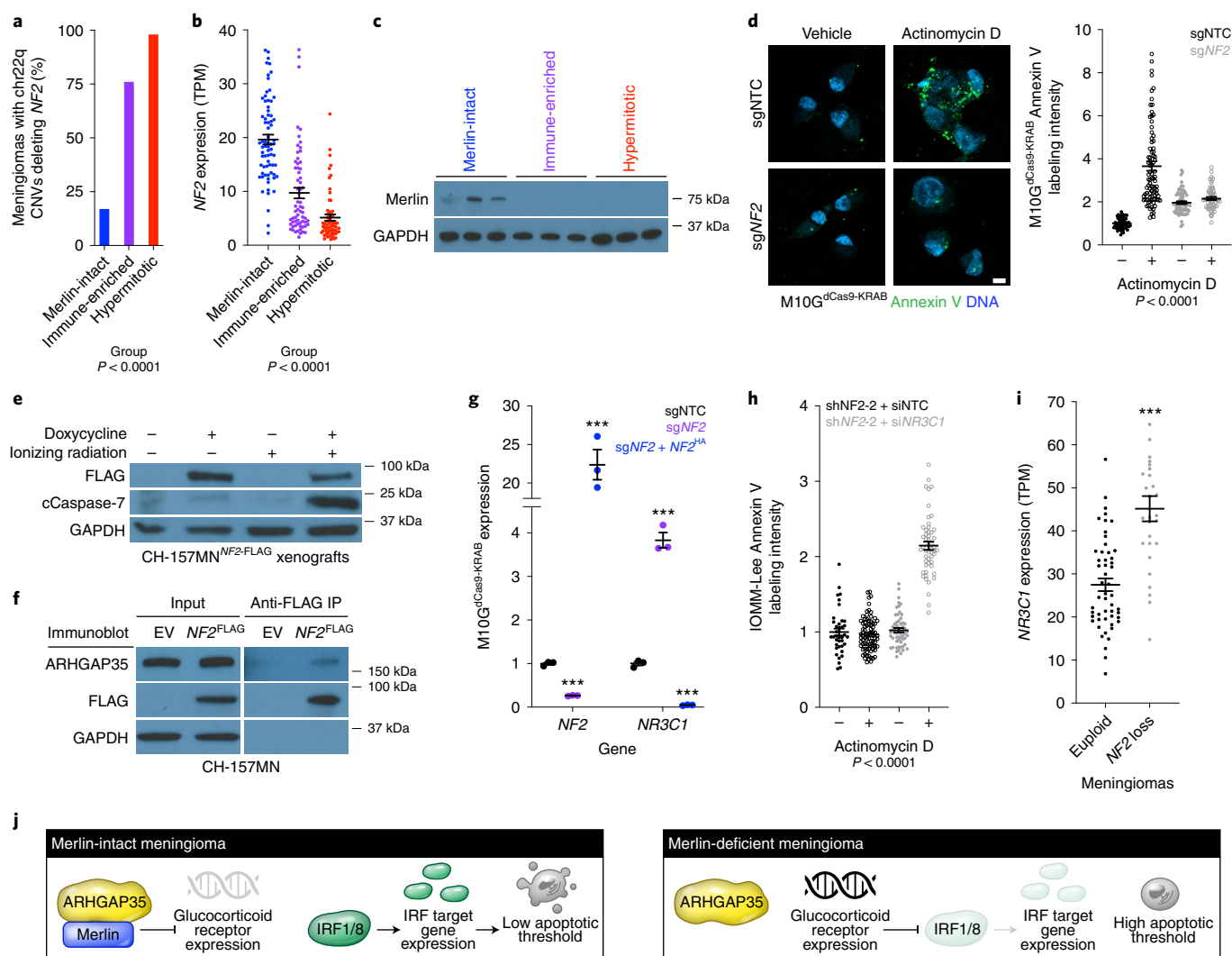
Fig. 2 | *NF2*/Merlin drives meningioma apoptosis and susceptibility to cytotoxic therapy. a, Meningioma DNA methylation analysis of chromosome 22q segment copy-number deletions of any size containing the entire *NF2* locus across Merlin-intact ($n=32$ of 192 meningiomas, 17%), Immune-enriched ($n=165$ of 216 meningiomas, 76%) or Hypermitotic ($n=154$ of 157 meningiomas, 98%) DNA methylation groups ($n=565$, chi-squared test, two sided). **b**, Meningioma *NF2* transcripts per million (TPM) expression across Merlin-intact ($n=72$), Immune-enriched ($n=65$) or Hypermitotic ($n=63$) DNA methylation groups ($n=200$, analysis of variance (ANOVA), one sided). **c**, Immunoblot for Merlin or GAPDH in three meningiomas with loss of at least one copy of the *NF2* locus from each meningioma DNA methylation group. **d**, Confocal microscopy and quantification of Annexin V in M10G$^{dCas9\text{-}KRAB}$ cells stably expressing a nontargeting control single-guide RNA (sgNTC) or a single-guide RNA suppressing *NF2* (sg*NF2*) after 24-h actinomycin D or vehicle control treatment. DNA is marked with 4,6-diamidino-2-phenylindole (DAPI). Scale bar, 10 μM. From left to right, 53, 88, 69 or 56 cells are shown (ANOVA, one sided). **e**, Immunoblot for FLAG, cleaved caspase-7 (cCaspase-7) or GAPDH from CH-157MN xenografts stably expressing doxycycline-inducible Merlin encoding a FLAG tag (*NF2*^{FLAG}) in NU/NU mice after 7 days of doxycycline or vehicle treatment and 24 h after 4-Gy ionizing radiation or control treatment. **f**, Immunoblot for ARHGAP35 or FLAG after FLAG immunoprecipitation (IP) from CH-157MN cells stably expressing Merlin encoding a FLAG tag (*NF2*^{FLAG}). EV, empty vector. **g**, Quantitative polymerase chain reaction (qPCR) for *NF2* or *NR3C1* in M10G$^{dCas9\text{-}KRAB}$ cells stably expressing sgNTC, sg*NF2* or sg*NF2* with *NF2* rescue (sg*NF2* + *NF2*^{HA}). Three biological replicates per condition (Student's *t*-test, one sided). **h**, Quantification of Annexin V confocal microscopy in IOMM-Lee cells stably expressing a short-hairpin RNA suppressing *NF2* (sh*NF2*-2) and transiently expressing a nontargeting control siRNA (siNTC) or siRNAs suppressing *NR3C1* (si*NR3C1*). Cells were treated as in **d**. From left to right, 39, 80, 58 or 52 cells are shown (ANOVA, one sided). **i**, *NR3C1* TPM expression in euploid meningiomas ($n=52$) or meningiomas with loss of *NF2* as the only CNV ($n=28$) (Student's *t*-test, one sided). **j**, Model of Merlin proapoptotic tumor suppressor function in meningiomas. Lines represent means, and error bars represent standard error of the means. ***$P \le 0.0001$.

($n=165$ of 216) or 98% ($n=154$ of 157) of meningiomas in the DNA methylation groups with intermediate or poor outcomes, respectively (Fig. 2a and Supplementary Table 2). RNA sequencing of 200 meningiomas from the discovery cohort confirmed higher *NF2* expression in the DNA methylation group with the best outcomes compared to other groups (Fig. 2b). The combined distribution of *NF2* copy-number deletions and somatic short variants

from DNA amplicon sequencing of 65 meningiomas showed 89% of tumors in the DNA methylation group with the best outcomes encoded at least 1 wild-type copy of *NF2* (Extended Data Fig. 4a and Supplementary Table 3). An orthogonal comparison of meningiomas with deletion of at least 1 copy of *NF2* revealed Merlin protein was only expressed in the DNA methylation group with the best outcomes (Fig. 2c).

NF2 variants are mutually exclusive from *TRAF7* somatic short variants in meningiomas[11,13,16], and *TRAF7* variants were enriched in Merlin-intact meningiomas compared to other groups (Supplementary Table 4). Many Merlin-intact meningiomas did not encode *TRAF7* variants (79%), suggesting the DNA methylation group with the best outcomes may not be unified by a single genetic driver. Indeed, meningioma histologic subtypes associated with *AKT1*[E17K] variants were enriched in Merlin-intact meningiomas compared to tumors from other groups[17] (Supplementary Table 4). Further, analysis of matched exome sequencing and DNA methylation profiling on 53 meningiomas revealed no solitary *TRAF7, AKT1, KLF4* or other somatic short variants associated with favorable outcomes[4,13,17,18] in DNA methylation groups with intermediate or poor outcomes (Supplementary Table 5).

Merlin has myriad tumor suppressor functions in schwannoma cells[19–21], but Merlin tumor suppressor functions in meningiomas are incompletely understood. M10G and IOMM-Lee meningioma cells express Merlin[22,23], which inhibits cell proliferation in these cells (Extended Data Fig. 4b–f). To identify gene expression programs underlying Merlin tumor suppressor functions in meningioma cells, RNA sequencing was performed on triplicate M10G cultures stably expressing the CRISPR interference (CRISPRi) components dCas9-KRAB[24,25] and nontargeting control single-guide RNA (sgRNA) (sgNTC), sgRNA suppressing *NF2* (sg*NF2*), or sg*NF2* with *NF2* rescue (Extended Data Fig. 4c). Differential expression and ontology analyses revealed Merlin induced proapoptotic interferon regulatory factor (IRF) pathways (Extended Data Fig. 4g,h and Supplementary Table 6). Merlin suppression blocked IRF target gene expression in MSC1 cells[22] (Extended Data Fig. 4i,j), whose DNA methylation profiles were assigned as Merlin-intact using the multiclass support vector machine classifier. Thus, to determine if Merlin regulates meningioma cell apoptosis, MSC1, M10G[dCas9-KRAB], or IOMM-Lee cultures were treated with the chemotherapy agent actinomycin D, revealing Merlin suppression reduced apoptosis (Fig. 2d and Extended Data Fig. 5a–c). To define the relevance of this mechanism in vivo, CH-157MN meningioma cells, which do not express Merlin[26], were grown as xenografts harboring an inducible Merlin construct. Merlin rescue in CH-157MN xenografts increased apoptosis in response to ionizing radiation compared to meningiomas lacking Merlin (Fig. 2e and Extended Data Fig. 5d).

Merlin regulates protein degradation to control schwannoma cell proliferation[21], but Merlin suppression did not alter IRF stability or subcellular localization in meningioma cells (Extended Data Fig. 5e). To determine if Merlin instead regulates IRF activity, Merlin constructs encoding ascorbic acid peroxidase (APEX) tags were expressed in meningioma cells for proximity-labeling proteomic mass spectrometry[27] (Supplementary Table 7). ARHGAP35, a DNA binding factor that inhibits glucocorticoid receptor expression[28,29], was detected in proximity to wild-type Merlin, but not Merlin[L46R], a missense variant associated with neurofibromatosis type 2 (ref. [21]) (Extended Data Fig. 5f). Glucocorticoid signaling inhibits IRF activity to prevent apoptosis[30,31], and immunoprecipitation of Merlin from meningioma cells validated Merlin interaction with ARHGAP35 (Fig. 2f). IRF proteins were not detected in proximity to Merlin[APEX] constructs (Supplementary Table 7) or in Merlin immunoprecipitates (Extended Data Fig. 5g), suggesting Merlin indirectly regulates IRF activity through ARHGAP35. In support of this hypothesis, *NF2* suppression in meningioma cells induced glucocorticoid receptor expression, which was inhibited by *NF2* rescue (Fig. 2g). Further, glucocorticoid receptor suppression rescued meningioma cell apoptosis in the absence of Merlin (Fig. 2h and Extended Data Fig. 5h), and glucocorticoid receptor expression was increased in human meningiomas with *NF2* loss compared to euploid tumors (Fig. 2i). In sum, these data shed light on a proapoptotic tumor suppressor function of Merlin regulating glucocorticoid signaling and susceptibility to cytotoxic therapy in meningiomas (Fig. 2j).

Convergent mechanisms underlie meningioma immune enrichment

Meningiomas in the DNA methylation group with intermediate outcomes had fewer CNVs than other groups (Supplementary Fig. 3b), suggesting bulk bioinformatic analyses of meningiomas in this group may be influenced by nontumor cells in the meningioma microenvironment (Supplementary Table 8). SeSAMe cell-type deconvolution of DNA methylation profiles showed immune cell enrichment in the meningioma DNA methylation group with intermediate outcomes compared to other groups (Fig. 3a). xCell RNA sequencing deconvolution and PAMES tumor purity analysis validated these findings[32,33] (Supplementary Fig. 4a–d). Further, differential expression and gene ontology analyses showed enrichment of immune genes in the meningioma DNA methylation group with intermediate outcomes (Supplementary Fig. 4e and Supplementary Table 9), and immunohistochemistry revealed T cell enrichment in this group compared to tumors from other groups (Fig. 3b). Differential expression and gene ontology analyses across minfi groups failed to distinguish meningiomas by immune or inflammatory gene expression programs (Supplementary Fig. 4f).

To define the cellular architecture of meningiomas, single-cell RNA sequencing was performed on 57,114 cells from eight meningioma samples with each DNA methylation group represented (Fig. 3c and Supplementary Fig. 5). Reduced dimensionality clusters of meningioma and non-meningioma cells were distinguished by chromosome 22q loss using CONICSmat[34] (Supplementary Fig. 6a). Nonmeningioma cell clusters with intact chromosome 22q were classified by expression of immune, neural, or vascular marker genes (Supplementary Fig. 6b,c and Supplementary table 10). Meningioma cell clusters with chromosome 22q loss were distinguished by differentially expressed cellular pathways or meningioma marker genes (Supplementary Figs. 5c and 6b,c and Supplementary Table 10). Single-cell transcriptomes revealed more immune cells in Immune-enriched meningiomas compared to tumors from other groups (Fig. 3d). Further, analysis of DNA methylation profiles on 86 spatially distinct samples from 13 meningiomas revealed 92% of samples classified in concordance with the consensus DNA methylation group of each tumor[22] (Supplementary Fig. 7a), suggesting meningioma DNA methylation grouping is not confounded by intratumor heterogeneity or spatial sampling bias.

Single-cell transcriptomes demonstrated increased expression of *HLA-DRB5, HLA-DRB1, HLA-DQA1, HLA-DQB1, HLA-DMA* and *HLA-DPB1* in Immune-enriched meningioma cells compared to meningioma cells from other groups (Fig. 3e). *HLA* loss on chromosome 6p can decrease immune infiltration in cancer[35], and there was a polymorphic locus on chromosome 6p encompassing *HLA-DRB5, HLA-DRB1, HLA-DQA1* and *HLA-DQB1*, with recurrent gains or losses across meningioma DNA methylation groups (Fig. 1a, Supplementary Fig. 3a and Supplementary Table 2). Copy-number amplifications of any size containing the entire polymorphic *HLA* locus were more frequent in Immune-enriched meningiomas (17%, $n = 37$ of 216) compared to Merlin-intact (11%, $n = 21$ of 192) or Hypermitotic meningiomas (12%, $n = 12$ of 157) ($P = 0.0174$, chi-squared test) (Fig. 3f). Conversely, copy-number deletions of any size containing the entire polymorphic *HLA* locus were less frequent in Immune-enriched meningiomas (8%, $n = 18$ of 216) compared to Merlin-intact (15%, $n = 28$ of 192) or Hypermitotic meningiomas (20%, $n = 32$ of 157) ($P = 0.0036$, chi-squared test) (Fig. 3f). Analysis of matched whole-exome sequencing and DNA methylation profiling revealed no instances of *HLA* loss of heterozygosity in Immune-enriched meningiomas[2] (Supplementary Fig. 7b). Expression of *HLA-DRB5, HLA-DRB1, HLA-DQA1* or *HLA-DQB1* correlated with CNVs amplifying or deleting these
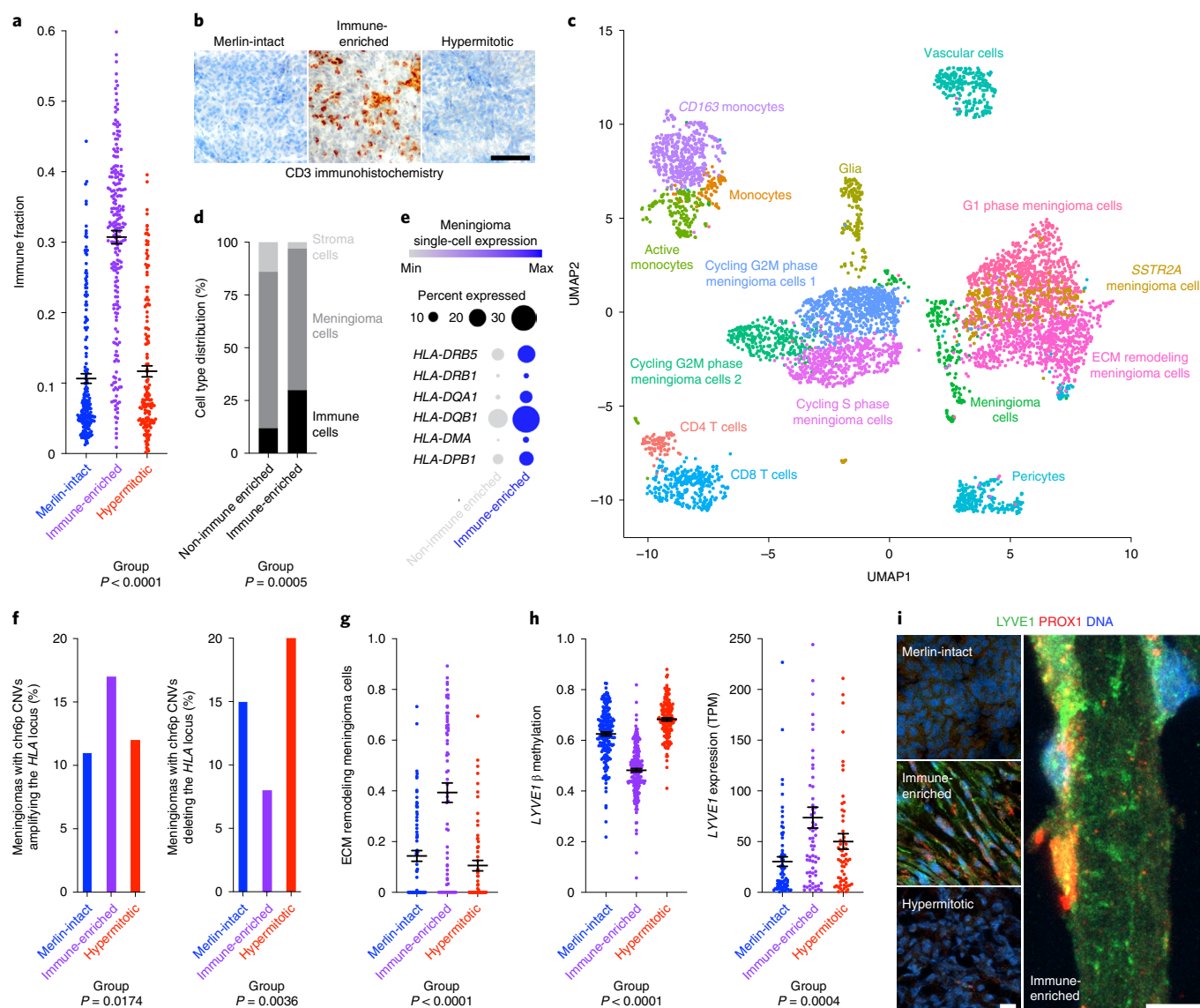
Fig. 3 | *HLA* expression and meningeal lymphatics underlie meningioma immune enrichment. a, Meningioma DNA methylation leukocyte fractions ($n=565$) across DNA methylation groups (ANOVA, one sided). **b**, Representative images of T cell immunohistochemistry across meningioma DNA methylation groups ($n=87$, $P<0.0001$, chi-squared test, two sided). Scale bar, 100 μM. **c**, Uniform manifold approximation and projection (UMAP) of single-cell RNA sequencing transcriptomes of 57,114 cells from 8 human meningioma samples and 2 human dura samples, colored by assignments from Louvain clustering. **d**, Quantification of single-cell types from **c** in Immune-enriched ($n=5$) and non-Immune-enriched ($n=3$) meningioma samples (chi-squared test, two sided). **e**, Single-cell RNA sequencing relative expression of *HLA* genes in meningioma cells across Immune-enriched ($n=5$) or non-Immune-enriched ($n=3$) meningioma samples. Circle size denotes percentage of cells. Shading denotes average expression. **f**, Meningioma DNA methylation analysis of chromosome 6p segment CNVs containing the entire polymorphic *HLA* locus encompassing *HLA-DRB5, HLA-DRB1, HLA-DQA1* and *HLA-DQB1* across Merlin-intact ($n=192$ meningiomas, 21 gains, 28 losses), Immune-enriched ($n=216$ meningiomas, 37 gains, 18 losses) or Hypermitotic ($n=157$ meningiomas, 12 gains, 32 losses) DNA methylation groups (chi-squared test, two sided). **g**, Fraction of meningioma samples ($n=200$) classified as extracellular matrix (ECM) remodeling meningioma cells across DNA methylation groups, based on single-cell reference transcriptomes from **c** (ANOVA, one sided). **h**, Meningioma DNA methylation ($n=565$) of *LYVE1* (cg26455970) and transcripts per million (TPM) expression ($n=200$) of *LYVE1* across DNA methylation groups (ANOVA, one sided). **i**, Representative images of meningioma LYVE1 and PROX1 immunofluorescence microscopy across DNA methylation groups ($n=12$). DNA is marked with Hoechst 33342. Scale bars, 10 μM. Lines represent means, and error bars represent standard error of the means.

genes, and the expression of *HLA-DRB5, HLA-DRB1, HLA-DQA1* or *HLA-DQB1* was enriched in Immune-enriched meningiomas compared to other groups (Supplementary Fig. 7c). *HLA-DMA* and *HLA-DPB1*, located outside the polymorphic locus on chromosome 6p, had increased expression in single-cell transcriptomes from Immune-enriched meningioma cells (Fig. 3e) and were hypomethylated with increased expression in Immune-enriched

meningiomas compared to other groups (Supplementary Fig. 7d–f). In sum, these data reveal convergent genetic and epigenetic mechanisms underlying meningioma *HLA* expression.

To identify additional mechanisms underlying Immune-enriched meningiomas, reference transcriptomic signatures of meningioma single-cell clusters were generated using CIBERSORTx (ref. [36]), and cell-type proportions across meningioma DNA methylation groups
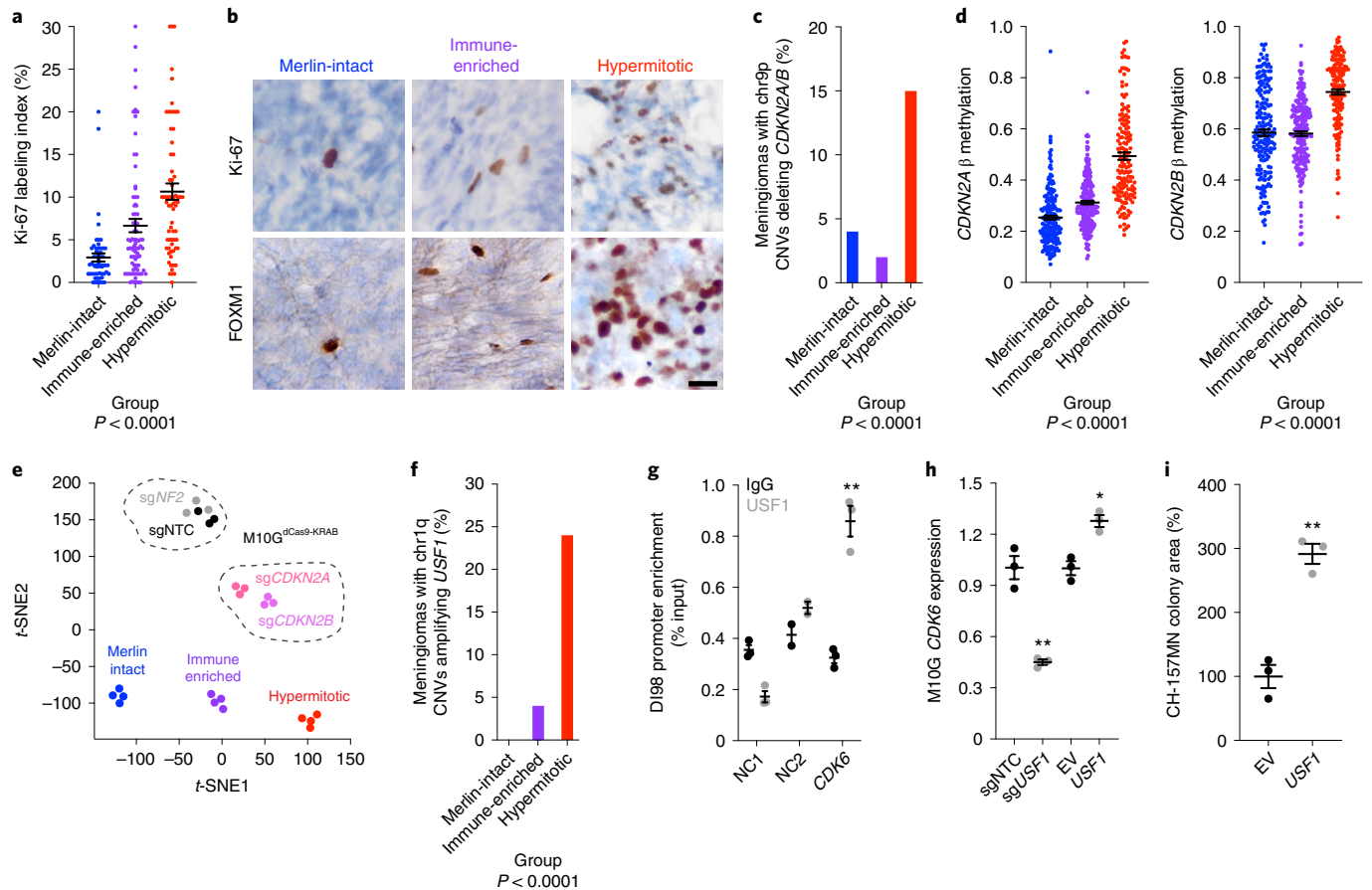
Fig. 4 | Convergent genetic and epigenetic mechanisms misactivate the cell cycle in meningioma. a, Ki-67 labeling index from meningioma clinical pathology reports ($n=206$) across DNA methylation groups (ANOVA, one sided). **b**, Representative images of meningioma Ki-67 and FOXM1 immunohistochemistry ($n=92$) across meningioma DNA methylation groups. Scale bar, 10 μM. **c**, Meningioma DNA methylation analysis of chromosome 9p segment copy-number deletions of any size containing the entire *CDKN2A/B* locus across Merlin-intact ($n=8$ of 192 meningiomas, 4%), Immune-enriched ($n=5$ of 216 meningiomas, 2%) or Hypermitotic ($n=24$ of 157 meningiomas, 15%) DNA methylation groups ($n=565$, chi-squared test, two sided). **d**, Meningioma DNA methylation ($n=565$) of *CDKN2A* (cg26349275) or *CDKN2B* (cg08390209) across DNA methylation groups (ANOVA, one sided). **e**, t-Distributed stochastic neighbor embedding (t-SNE) plot of meningioma or meningioma cell line DNA methylation profiles. Four representative meningiomas from each DNA methylation group are shown. Triplicate meningioma M10G[dCas9-KRAB] cultures stably expressing a non-targeting control sgRNA (sgNTC) or sgRNAs suppressing *NF2* (sg*NF2*), *CDKN2A* (sg*CDKN2A*) or *CDKN2B* (sg*CDKN2B*) are shown. Differences in DNA methylation groups are captured in t-SNE1, and a positive shift from Immune-enriched meningiomas to Hypermitotic meningiomas mimics the shift from M10G[dCas9-KRAB]-sgNTC or M10G[dCas9-KRAB]-sg*NF2* cells to M10G[dCas9-KRAB]-sg*CDKN2A* or M10G[dCas9-KRAB]-sg*CDKN2B* cells. Differences between tumors and cell lines, such as the tumor microenvironment, are captured in t-SNE2. **f**, Meningioma DNA methylation analysis of chromosome 1q segment copy-number amplifications of any size containing the entire *USF1* locus across Merlin-intact ($n=0$ of 192 meningiomas, 0%), Immune-enriched ($n=2$ of 216 meningiomas, 4%) or Hypermitotic ($n=38$ of 157 meningiomas, 24%) DNA methylation groups ($n=565$, chi-squared test, two sided). **g**, USF1 ChIP-qPCR in DI-98 meningioma cells for the *CDK6* promoter compared to negative control primers targeting a gene desert (NC1) or a gene not predicted to be bound by USF1 (NC2) from ChIP sequencing. **$P=0.001$ (Student's t-test, one sided, no adjustment for multiple comparisons). **h**, qPCR for *CDK6* in M10G[dCas9-KRAB] cells expressing sgNTC or an sgRNA suppressing *USF1* (sg*USF1*), or for *CDK6* in M10G cells overexpressing *USF1* or empty vector (EV). *$P=0.003$, **$P=0.001$ (Student's t-test, one sided, no adjustment for multiple comparisons). **i**, Relative colony area of CH-157MN cells stably overexpressing USF1 or EV after 10 days of clonogenic growth. **$P=0.001$ (Student's t-test, one sided, no adjustment for multiple comparisons). Lines represent means, and error bars represent standard error of the means.

were deconvolved from RNA sequencing of the discovery cohort (Extended Data Fig. 6a). Changes in the extracellular matrix can create a permissive microenvironment for lymphatic vessel formation[37–40] and we observed meningioma cells expressing extracellular matrix remodeling genes were enriched in Immune-enriched meningiomas compared to tumors from other groups (Fig. 3g). Consistently, DNA methylation probes that were hypomethylated in Immune-enriched meningiomas compared to other groups were concentrated at genes involved in vasculature, vessel, or circulatory system development (Supplementary Table 8). Meningeal lymphatics near dural venous sinuses are necessary for central nervous

system immune surveillance[41–45], but preoperative magnetic resonance imaging showed meningiomas from multiple DNA methylation groups were likely to involve dural venous sinuses (Extended Data Fig. 6b,c), suggesting meningioma location may be necessary but not sufficient for immune infiltration. Compared to tumors from other DNA methylation groups, Immune-enriched meningiomas had hypomethylation and increased expression of meningeal lymphatic genes such as *LYVE1*, *CCL21* or *CD3E*[44,46–48] (Fig. 3h and Extended Data Fig. 6d,e). Immunofluorescence confirmed lymphatic enrichment in Immune-enriched meningiomas compared to tumors from other groups (Fig. 3i) and also in CH-157MN

xenografts (Extended Data Fig. 6f), whose DNA methylation profiles were assigned as Immune-enriched using the multiclass support vector machine classifier. Thus, *HLA* expression and lymphatic vessels are associated with meningioma immune infiltration.

Convergent mechanisms misactivate the meningioma cell cycle

High-grade meningiomas are defined by brisk cell proliferation leading to local recurrence and death in 50%–90% of patients[49,50], and cell proliferation was highest in the meningioma DNA methylation group with the worst clinical outcomes (Fig. 4a). To elucidate mechanisms driving cell proliferation in Hypermitotic meningiomas, RNA sequencing, gene ontology analysis and immunohistochemistry revealed FOXM1 and the FOXM1 gene expression program were enriched in Hypermitotic meningiomas compared to tumors from other groups (Fig. 4b, Supplementary Fig. 8a and Supplementary Table 9), correlating with meningioma cell proliferation (Supplementary Fig. 8b,c). FOXM1 is a biomarker for meningioma recurrence and drives cell proliferation, and putative FOXM1 target genes are accessible in the chromatin of meningioma DNA methylation groups with adverse clinical outcomes[2,7,51,52]. To define the specificity of FOXM1 signaling across meningioma DNA methylation groups, differential expression and ontology analyses were compared between Hypermitotic meningiomas with elevated Ki-67 labeling index and non-Hypermitotic meningiomas with elevated Ki-67 labeling index, revealing the FOXM1 gene expression program was specifically enriched in Hypermitotic meningiomas (Supplementary Fig. 8d). Although many FOXM1 targets are induced by other cell cycle regulators, such as E2F1 (ref. [53]), FOXM1 targets nonoverlapping with E2F1 targets were enriched in Hypermitotic meningiomas compared to tumors from other groups (Supplementary Fig. 8e), and E2F1 targets nonoverlapping with FOXM1 targets did not distinguish meningioma DNA methylation groups (Supplementary Fig. 9). To elucidate the function of FOXM1 target genes in Hypermitotic meningiomas, differentially expressed genes with FOXM1 binding motifs were analyzed across 25 meningiomas with matched RNA sequencing, H3K27ac chromatin immunoprecipitation (ChIP) sequencing and DNA methylation profiling[54]. FOXM1 targets in Hypermitotic meningiomas regulated the cell cycle, tumor metabolism and the DNA damage response (Extended Data Fig. 7a), suggesting FOXM1 may underlie Hypermitotic meningioma resistance to cytotoxic therapy. In support of this hypothesis, FOXM1 protein increased in meningioma cells treated with actinomycin D (Extended Data Fig. 7b), and overexpression of FOXM1 increased meningioma cell resistance to cytotoxic chemotherapy (Extended Data Fig. 7c,d).

H3K27ac ChIP sequencing analysis of enhancer or superenhancer availability showed Hypermitotic meningiomas were dominated by epigenetic regulators and transcription factors that are impractical pharmacologic targets (Supplementary Fig. 10). More broadly, druggable somatic short variants in meningiomas are rare and are not associated with adverse clinical outcomes[1,10–14,16,17,51,55–58], with infrequent exceptions[59–62]. There were more CNVs in Hypermitotic meningiomas compared to other groups (Supplementary Fig. 3a,b), and chromosome instability drives cancer evolution and response to therapy[63–65]. Thus, we hypothesized CNVs contributing to cell cycle misactivation may harbor therapeutic vulnerabilities informing new treatments for meningioma patients.

Loss of the endogenous CDK4/6 inhibitor *CDKN2A/B* on chromosome 9p is a rare biomarker for meningioma recurrence[62,66]. Copy-number deletions of any size containing the entire *CDKN2A/B* locus were identified in 6.5% of meningiomas ($n = 37$ of 565) but were enriched in Hypermitotic meningiomas (15%, $n = 24$ of 157) compared to Merlin-intact (4%, $n = 8$ of 192) or Immune-enriched meningiomas (2%, $n = 5$ of 216) (Fig. 4c and Supplementary
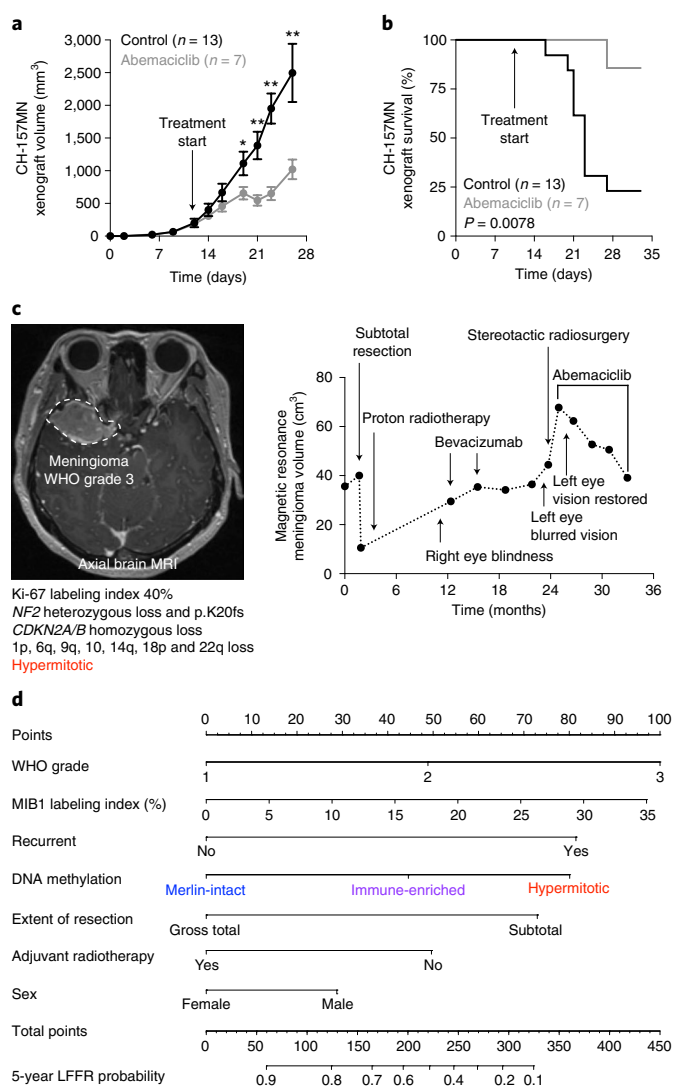
**Fig. 5 | Clinical translation of meningioma DNA methylation groups.** **a**, Subcutaneous CH-157MN xenograft measurements in NU/NU mice treated with abemaciclib (100 µg g⁻¹) by daily oral gavage with versus control. Lines represent means, and error bars represent standard error of the means. *$P \leq 0.05$, **$P \leq 0.01$ (Student's *t*-test, one sided). **b**, Kaplan–Meier curve for CH-157MN xenograft OS in NU/NU mice treated as in **a** (log-rank test). **c**, Magnetic resonance imaging and molecular features of a representative human meningioma (left) that was resistant to cytotoxic therapies but responded to cytostatic cell cycle inhibition (right). **d**, Nomogram for meningioma LFFR ($n = 201$) integrating clinical features and DNA methylation groups. Variables contribute points (top row), which estimate the probably of 5-year LFFR (bottom rows) (https://william-c-chen.shinyapps.io/RaleighLab_MethylationSubgroupNomogram/).

Table 2) and were associated with worse LFFR (Supplementary Fig. 11a). *CDKN2A/B* hypermethylation, an alternate mechanism of cell cycle misactivation in cancer[67,68], was also more frequent in Hypermitotic meningiomas compared to other groups (Fig. 4d). Stable suppression of *CDKN2A* or *CDKN2B* increased M10G^(dCas9-KRAB) cell proliferation (Supplementary Fig. 11b,c) and reassigned M10G^(dCas9-KRAB) DNA methylation profiles from Immune-enriched to Hypermitotic using the multiclass support vector machine classifier. *t*-SNE visualization of M10G^(dCas9-KRAB) DNA methylation profiles in the context of Merlin-intact, Immune-enriched or Hypermitotic
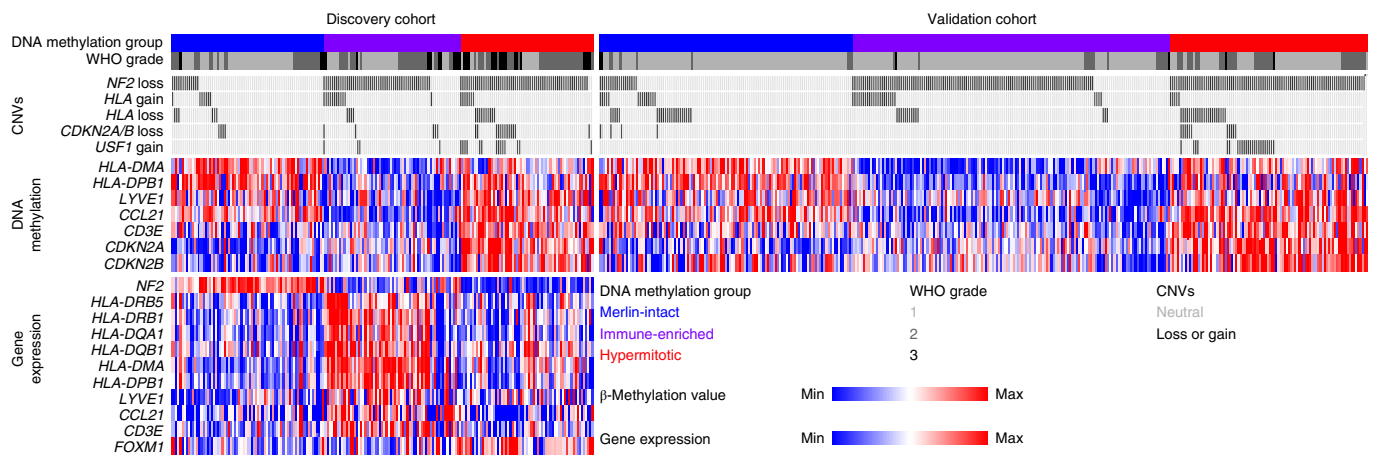
Fig. 6 | Genetic, epigenetic and transcriptomic mechanisms distinguishing meningioma DNA methylation groups. Oncoprint composed of the 565 meningiomas in this study. CNVs of any size deleting or amplifying entire genes, scaled β-methylation values, or scaled transcripts per million (TPM) are shown. The focal versus broad nature of CNVs are described in the copy-number analysis section of Methods. *HLA* gain/loss shows the polymorphic locus encompassing *HLA-DRB5*, *HLA-DRB1*, *HLA-DQA1* and *HLA-DQB1*. β-methylation values or TPM were scaled from the bottom 10th percentile to the top 90th percentile of each row. RNA sequencing was performed on the discovery cohort ($n = 200$), but not on the validation cohort.

meningiomas also revealed a shift in the DNA methylation profiles of M10G$^{dCas9-KRAB}$ cells from Immune-enriched to Hypermitotic meningiomas (Fig. 4e).

Most Hypermitotic meningiomas did not have CNVs deleting *CDKN2A/B* (Fig. 4c) or misactivation of the FOXM1 gene expression program (Supplementary Fig. 8e), and clustering of meningioma transcriptomes was unable to identify a unifying mechanism underlying Hypermitotic meningiomas (Supplementary Fig. 12). Thus, to identify additional mechanisms driving the cell cycle in meningiomas, transcription factor binding sites were mapped to regions of open chromatin defined by H3K27ac ChIP sequencing, revealing a binding site for the poorly understood transcription factor USF1 in the *CDK6* promoter in meningiomas (Supplementary Fig. 13a and Supplementary Table 11). Chromosome 1q copy-number amplifications of any size containing the entire *USF1* locus were enriched in Hypermitotic meningiomas (24%, $n = 38$ of 157) compared to Merlin-intact (0%, $n = 0$ of 192) or Immune-enriched meningiomas (2%, $n = 4$ of 216) (Fig. 4f and Supplementary Table 2) and were associated with worse LFFR (Supplementary Fig. 13b). Mechanistic studies showed USF1 bound and activated the *CDK6* promoter in Hypermitotic meningioma cells (Fig. 4g,h and Supplementary Fig. 13c, d), and USF1 overexpression increased non-Hypermitotic meningioma cell proliferation (Fig. 4i and Supplementary Fig. 13e).

To define the distribution of genetic and epigenetic mechanisms misactivating the cell cycle in Hypermitotic meningiomas, *CDKN2A/B* methylation (Fig. 4d) or *FOXM1* expression (Extended Data Fig. 7 and Supplementary Fig. 8) in the top quartile of meningiomas was analyzed alongside CNVs of any size deleting the entire *CDKN2A/B* locus (Fig. 4c) or amplifying the entire *USF1* locus (Fig. 4f). Among the 63 Hypermitotic meningiomas in the discovery cohort (Supplementary Table 1), there were 13 tumors with CNVs deleting *CDKN2A/B*, 14 tumors with CNVs amplifying *USF1*, 37 tumors with *CDKN2A* hypermethylation, 32 tumors with *CDKN2B* hypermethylation and 26 tumors with increased *FOXM1* expression (Supplementary Table 12). Removing duplicates, 52 of 63 Hypermitotic meningiomas in the discovery cohort had *CDKN2A/B* deletion, *USF1* amplification, *CDKN2A/B* hypermethylation or increased expression of *FOXM1* (83%). Multiple genetic, epigenetic or transcriptomic mechanisms misactivating the cell cycle were identified in 40 of 63 Hypermitotic meningiomas (63%).

Clinical translation of meningioma DNA methylation groups

Merlin regulation of glucocorticoid signaling drives meningioma apoptosis (Fig. 2j), and Merlin-intact meningiomas have the best clinical outcomes with current therapies (Fig. 1c and Supplementary Fig. 2a). In contrast, Immune-enriched and Hypermitotic meningiomas have adverse outcomes (Fig. 1c and Supplementary Fig. 2a), elevated cell proliferation (Fig. 4a), and are resistant to cytotoxic therapies due to loss of Merlin (Fig. 2j) or misactivation of FOXM1 (Extended Data Fig. 7). The convergence of mechanisms driving cytotoxic resistance and cell cycle misactivation in Immune-enriched and Hypermitotic meningiomas suggests cytostatic cell cycle inhibitors may be effective treatments for meningiomas from these DNA methylation groups. To test this hypothesis, the CDK4/6 inhibitors abemaciclib, palbociclib and ribociclib were studied in cell culture, organoids, or xenografts using Immune-enriched or Hypermitotic meningioma cells. CDK4/6 inhibitors blocked clonogenic growth of meningioma cells without cell cycle modifications (Extended Data Fig. 8a), but suppression of *CDKN2A/B* or overexpression of *USF1* increased meningioma cell sensitivity to cell cycle inhibitors (Extended Data Fig. 8b,c). To test this therapeutic strategy in the context of a tumor microenvironment, meningioma cells were co-cultured with cerebral organoids comprised of predifferentiated human pluripotent stem-cell derived astrocytes. This model recapitulates intratumor heterogeneity in meningioma cells[22], and intratumor heterogeneity drives resistance to therapy[69], but CDK4/6 inhibition nevertheless attenuated meningioma cell growth in organoid co-cultures (Extended Data Fig. 8d). To define the pharmacodynamics and efficacy of this strategy for meningiomas in vivo, CH-157MN xenografts were treated with CDK4/6 inhibitors, which decreased RB phosphorylation (Extended Data Fig. 8e), inhibited cell proliferation (Extended Data Fig. 8f), attenuated xenograft growth (Fig. 5a) and prolonged survival (Fig. 5b).

These data provide preclinical rationale to treat patients with Immune-enriched or Hypermitotic meningiomas with cell cycle inhibitors, which achieve therapeutic doses in human meningiomas[70]. In support of these preclinical investigations, we have observed encouraging early results with compassionate use of CDK4/6 inhibitors in patients with Hypermitotic meningiomas that are resistant to surgery and radiotherapy (Fig. 5c and Supplementary Fig. 14). Clinical trials to establish the efficacy of this and other molecular therapies for meningiomas will require rigorous patient
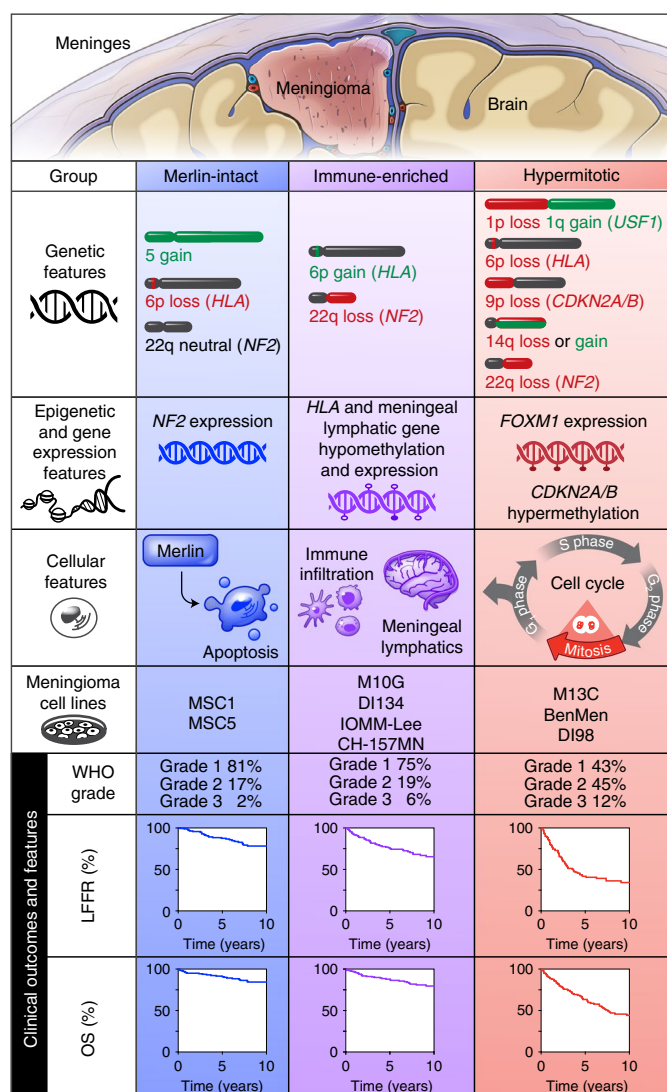
Fig. 7 | Molecular, cellular and clinical features distinguishing meningioma DNA methylation groups. DNA methylation profiling was performed on 565 meningiomas and integrated with genetic, transcriptomic, biochemical, proteomic and single-cell approaches to show meningiomas are composed of three DNA methylation groups with distinct clinical outcomes, biological drivers and therapeutic vulnerabilities. DNA methylation profiling was also performed on nine meningioma cell lines to define reagents to study biological drivers and therapeutic vulnerabilities underlying meningioma DNA methylation groups.

selection and biological stratification. In anticipation, we developed nomograms to compare models based on meningioma DNA methylation groups to models based on CNVs or clinical variables (Fig. 5d and Supplementary Figs. 15 and 16).

Discussion

DNA methylation profiling is a powerful tool for biological discovery, but clinical adoption of this approach has been encumbered by a lack of medical indications. The data presented here demonstrate a need for DNA methylation profiling to stratify meningioma patients for molecular therapies. Integrating genetic, epigenetic, transcriptomic, biochemical, proteomic and single-cell approaches, we find meningiomas are composed of three DNA methylation groups with distinct clinical outcomes and biological drivers. We validate our

results using mechanistic and functional studies in cells, organoids, xenografts and patients to elucidate mechanisms underlying therapeutic resistance and susceptibility in the most common primary intracranial tumor.

Our study tests the hypothesis that controlling for the influence of CNVs on β-methylation values may reveal insights into meningioma biology. In support of this approach, meningioma DNA methylation analysis uncontrolled for the influence of CNVs on β-methylation values could not identify an optimal number of meningioma groups (Extended Data Fig. 3b,c) or groups with nonoverlapping differences in clinical outcomes, NF2 loss, immune enrichment, cell proliferation and chromosome instability (Extended Data Figs. 3d and 9). Quantifying the signal-to-noise ratio of NF2 loss across meningioma DNA methylation groups, we found a signal-to-noise ratio of 5.57 for three SeSAMe groups compared to 2.25 for three minfi groups.

Integrating epigenetic or gene expression features alongside genetic alterations may be important for understanding the biology of meningioma DNA methylation groups (Fig. 6). We identified CNVs of any size deleting the entire CDKN2A/B locus or amplifying the entire USF1 locus in 54 of 157 Hypermitotic meningiomas (35%) (Supplementary Table 2), but when integrated with CDKN2A/B hypermethylation and FOXM1 expression, the genetic, epigenetic, and transcriptomic alterations underlying meningioma cell proliferation we report were found in 83% of Hypermitotic tumors (Supplementary Table 12). We used the same approach to integrate CNVs of any size amplifying the entire polymorphic HLA locus with hypomethylation of HLA-DMA, HLA-DPB1 or meningeal lymphatic genes (LYVE1, CCL21 and CD3E) (Supplementary Table 13). Removing duplicates, the epigenetic and genetic alterations underlying meningioma immune infiltration we report were found in 166 of 216 Immune-enriched meningiomas (77%). Multiple genetic or epigenetic mechanisms underlying immune infiltration were identified in 157 of 216 Immune-enriched meningiomas (73%).

Our mechanistic and functional studies validate a biomarker-based treatment for meningiomas with adverse clinical outcomes. We find Immune-enriched meningiomas display multiple markers of immunoediting, and T cells in the meningioma microenvironment display multiple markers of exhaustion (Extended Data Fig. 10). These data suggest immune checkpoint inhibition may be ineffective for Immune-enriched meningiomas and shed light on why meningioma immune infiltration does not correlate with improved clinical outcomes[71], as it does in other cancers[72]. Thus, we encourage careful consideration of meningioma DNA methylation groups in the context of available preclinical data, and WHO grade, when stratifying meningioma patients for new treatments. Indeed, our data demonstrate DNA methylation grouping does not obviate the importance of meningioma grading (Fig. 1e and Supplementary Fig. 2e). These complementary systems provide independent information about meningioma outcomes, but unlike WHO grade, the meningioma DNA methylation groups we report reveal biological drivers and therapeutic vulnerabilities informing new treatments for meningioma patients (Fig. 7).

Online content

Any methods, additional references, Nature Research reporting summaries, source data, extended data, supplementary information, acknowledgements, peer review information; details of author contributions and competing interests; and statements of data and code availability are available at https://doi.org/10.1038/s41588-022-01061-8.

References

1. Bi, W. L. et al. Genomic landscape of intracranial meningiomas. *J. Neurosurg.* **125**, 525–535 (2016).
2. Vasudevan, H. N. et al. Comprehensive molecular profiling identifies FOXM1 as a key transcription factor for meningioma proliferation. *Cell Rep.* **22**, 3672–3683 (2018).
3. Zhou, W., Triche, T. J., Laird, P. W. & Shen, H. SeSAMe: reducing artifactual detection of DNA methylation by Infinium BeadChips in genomic deletions. *Nucleic Acids Res.* **46**, e123–e123 (2018).
4. Sahm, F. et al. DNA methylation-based classification and grading system for meningioma: a multicentre, retrospective analysis. *Lancet Oncol.* **18**, 682–694 (2017).
5. Olar, A. et al. Global epigenetic profiling identifies methylation subgroups associated with recurrence-free survival in meningioma. *Acta Neuropathol.* **133**, 431–444 (2017).
6. Nassiri, F. et al. DNA methylation profiling to predict recurrence risk in meningioma: development and validation of a nomogram to optimize clinical management. *Neuro Oncol.* https://doi.org/10.1093/neuonc/noz061 (2019).
7. Harmancı, A. S. et al. Integrated genomic analyses of de novo pathways underlying atypical meningiomas. *Nat. Commun.* **8**, 14433 (2017).
8. Nassiri, F. et al. A clinically applicable integrative molecular classification of meningiomas. *Nature* **597**, 119–125 (2021).
9. Aryee, M. J. et al. Minfi: a flexible and comprehensive Bioconductor package for the analysis of Infinium DNA methylation microarrays. *Bioinformatics* **30**, 1363–1369 (2014).
10. Evans, Dg. R. Neurofibromatosis type 2 (NF2): a clinical and molecular review. *Orphanet J. Rare Dis.* **4**, 1–11 (2009).
11. Clark, V. E. et al. Genomic analysis of non-NF2 meningiomas reveals mutations in TRAF7, KLF4, AKT1, and SMO. *Science* **339**, 1077–1080 (2013).
12. Brastianos, P. K. et al. Genomic sequencing of meningiomas identifies oncogenic SMO and AKT1 mutations. *Nat. Genet.* **45**, 285–289 (2013).
13. Youngblood, M. W. et al. Correlations between genomic subgroup and clinical features in a cohort of more than 3000 meningiomas. *J. Neurosurg.* **1**, 1–10 (2019).
14. Agnihotri, S. et al. Therapeutic radiation for childhood cancer drives structural aberrations of NF2 in meningiomas. *Nat. Commun.* **8**, 186 (2017).
15. Sahm, F. et al. Meningiomas induced by low-dose radiation carry structural variants of NF2 and a distinct mutational signature. *Acta Neuropathol.* **134**, 155–158 (2017).
16. Reuss, D. E. et al. Secretory meningiomas are defined by combined KLF4 K409Q and TRAF7 mutations. *Acta Neuropathol.* **125**, 351–358 (2013).
17. Sahm, F. et al. AKT1E17K mutations cluster with meningothelial and transitional meningiomas and can be detected by SFRP1 immunohistochemistry. *Acta Neuropathol.* **126**, 757–762 (2013).
18. Findakly, S. et al. Meningioma cells express primary cilia but do not transduce ciliary Hedgehog signals. *Acta Neuropathologica Commun.* **8**, 114 (2020).
19. Curto, M., Cole, B. K., Lallemand, D., Liu, C.-H. & McClatchey, A. I. Contact-dependent inhibition of EGFR signaling by Nf2/Merlin. *J. Cell Biol.* **177**, 893–903 (2007).
20. Chiasson-MacKenzie, C. et al. NF2/Merlin mediates contact-dependent inhibition of EGFR mobility and internalization via cortical actomyosin. *J. Cell Biol.* **211**, 391–405 (2015).
21. Li, W. et al. Merlin/NF2 suppresses tumorigenesis by inhibiting the E3 ubiquitin ligase CRL4DCAF1 in the nucleus. *Cell* **140**, 477–490 (2010).
22. Magill, S. T. et al. Multiplatform genomic profiling and magnetic resonance imaging identify mechanisms underlying intratumor heterogeneity in meningioma. *Nat. Commun.* **11**, 4803 (2020).
23. Lee, W. H. Characterization of a newly established malignant meningioma cell line of the human brain: IOMM-Lee. *Neurosurgery* **27**, 389–396 (1990).
24. Gilbert, L. A. et al. Genome-scale CRISPR-mediated control of gene repression and activation. *Cell* **159**, 647–661 (2014).
25. Yeo, N. C. et al. An enhanced CRISPR repressor for targeted mammalian gene regulation. *Nat. Methods* **15**, 611–616 (2018).
26. Tsai, J.-C., Goldman, C. K. & Gillespie, G. Y. Vascular endothelial growth factor in human glioma cell lines: induced secretion by EGF, PDGF-BB, and bFGF. *J. Neurosurg.* **82**, 864–873 (1995).
27. Lobingier, B. T. et al. An approach to spatiotemporally resolve protein interaction networks in living cells. *Cell* **169**, 350–360.e12 (2017).
28. LeClerc, S., Palaniswami, R., Xie, B. X. & Govindan, M. V. Molecular cloning and characterization of a factor that binds the human glucocorticoid receptor gene and represses its expression. *J. Biol. Chem.* **266**, 17333–17340 (1991).
29. Leclerc, S., Xie, B. X., Roy, R. & Govindan, M. V. Purification of a human glucocorticoid receptor gene promoter-binding protein. Production of polyclonal antibodies against the purified factor. *J. Biol. Chem.* **266**, 8711–8719 (1991).
30. Flammer, J. R. et al. The type I interferon signaling pathway is a target for glucocorticoid inhibition. *Mol. Cell. Biol.* **30**, 4564–4574 (2010).
31. Ballegeer, M. et al. Glucocorticoid receptor dimers control intestinal STAT1 and TNF-induced inflammation in mice. *J. Clin. Invest.* **128**, 3265–3279 (2018).
32. Aran, D., Hu, Z. & Butte, A. J. xCell: digitally portraying the tissue cellular heterogeneity landscape. *Genome Biol.* **18**, 220 (2017).
33. Benelli, M., Romagnoli, D. & Demichelis, F. Tumor purity quantification by clonal DNA methylation signatures. *Bioinformatics* **34**, 1642–1649 (2018).
34. Müller, S., Cho, A., Liu, S. J., Lim, D. A. & Diaz, A. CONICS integrates scRNA-seq with DNA sequencing to map gene expression to tumor sub-clones. *Bioinformatics* **34**, 3217–3219 (2018).
35. McGranahan, N. et al. Allele-specific HLA loss and immune escape in lung cancer evolution. *Cell* **171**, 1259–1271.e11 (2017).
36. Newman, A. M. et al. Determining cell type abundance and expression from bulk tissues with digital cytometry. *Nat. Biotechnol.* **37**, 773–782 (2019).
37. Frye, M. et al. Matrix stiffness controls lymphatic vessel formation through regulation of a GATA2-dependent transcriptional program. *Nat. Commun.* **9**, 1511 (2018).
38. Zhang, X., Groopman, J. E. & Wang, J. F. Extracellular matrix regulates endothelial functions through interaction of VEGFR-3 and integrin alpha5beta1. *J. Cell. Physiol.* **202**, 205–214 (2005).
39. Vaahtomeri, K., Karaman, S., Mäkinen, T. & Alitalo, K. Lymphangiogenesis guidance by paracrine and pericellular factors. *Genes Dev.* **31**, 1615–1634 (2017).
40. Wiig, H., Keskin, D. & Kalluri, R. Interaction between the extracellular matrix and lymphatics: consequences for lymphangiogenesis and lymphatic function. *Matrix Biol.* **29**, 645–656 (2010).
41. Louveau, A. et al. Structural and functional features of central nervous system lymphatic vessels. *Nature* **523**, 337–341 (2015).
42. Antila, S. et al. Development and plasticity of meningeal lymphatic vessels. *J. Exp. Med.* **214**, 3645–3667 (2017).
43. Ahn, J. H. et al. Meningeal lymphatic vessels at the skull base drain cerebrospinal fluid. *Nature* **572**, 62–66 (2019).
44. Hu, X. et al. Meningeal lymphatic vessels regulate brain tumor drainage and immunity. *Cell Res.* **30**, 229–243 (2020).
45. Rustenhoven, J. et al. Functional characterization of the dural sinuses as a neuroimmune interface. *Cell* **184**, 1000–1016 (2021).
46. Banerji, S. et al. LYVE-1, a new homologue of the CD44 glycoprotein, is a lymph-specific receptor for hyaluronan. *J. Cell Biol.* **144**, 789–801 (1999).
47. Noor, S. & Wilson, E. H. Role of C-C chemokine receptor type 7 and its ligands during neuroinflammation. *J. Neuroinflammation* **9**, 77 (2012).
48. Wigle, J. T. et al. An essential role for Prox1 in the induction of the lymphatic endothelial cell phenotype. *EMBO J.* **21**, 1505–1513 (2002).
49. Louis, D. N. et al. The 2016 World Health Organization Classification of Tumors of the Central Nervous System: a summary. *Acta Neuropathol.* **131**, 803–820 (2016).
50. Rogers, L. et al. Meningiomas: knowledge base, treatment outcomes, and uncertainties. A RANO review. *J. Neurosurg.* **122**, 4–23 (2015).
51. Paramasivam, N. et al. Mutational patterns and regulatory networks in epigenetic subgroups of meningioma. *Acta Neuropathol.* **138**, 295–308 (2019).
52. Chen, W. C. et al. A prognostic gene-expression signature and risk score for meningioma recurrence after resection. *Neurosurgery* **88**, 202–210 (2020).
53. de Olano, N. et al. The p38 MAPK-MK2 axis regulates E2F1 and FOXM1 expression after epirubicin treatment. *Mol. Cancer Res.* **10**, 1189–1202 (2012).
54. Prager, B. C. et al. The meningioma enhancer landscape delineates novel subgroups and drives druggable dependencies. *Cancer Discov.* **10**, 1722–1741 (2020).
55. Clark, V. E. et al. Recurrent somatic mutations in POLR2A define a distinct subset of meningiomas. *Nat. Genet.* **48**, 1253–1259 (2016).
56. Sievers, P. et al. YAP1-fusions in pediatric NF2-wildtype meningioma. *Acta Neuropathol.* **139**, 215–218 (2020).
57. Williams, E. A. et al. Distinct genomic subclasses of high-grade/progressive meningiomas: NF2-associated, NF2-exclusive, and NF2-agnostic. *Acta Neuropathol. Commun.* **8**, 171 (2020).
58. Youngblood, M. W. et al. Associations of meningioma molecular subgroup and tumor recurrence. *Neuro Oncol.* **23**, 783–794 (2020).
59. Sahm, F. et al. TERT promoter mutations and risk of recurrence in meningioma. *J. Natl. Cancer Inst.* **108**, djv377 (2016).
60. Spiegl-Kreinecker, S. et al. TERT promoter mutations are associated with poor prognosis and cell immortalization in meningioma. *Neuro-Oncol.* **20**, 1584 (2018).
61. Shankar, G. M. & Santagata, S. BAP1 mutations in high-grade meningioma: implications for patient care. *Neuro-Oncol.* **19**, 1447 (2017).
62. Guyot, A. et al. Analysis of CDKN2A gene alterations in recurrent and non-recurrent meningioma. *J. Neurooncol.* **145**, 449–459 (2019).
63. Shoshani, O. et al. Chromothripsis drives the evolution of gene amplification in cancer. *Nature* **591**, 137–141 (2021).
64. Cohen-Shahir, Y. et al. Aneuploidy renders cancer cells vulnerable to mitotic checkpoint inhibition. *Nature* **590**, 486–491 (2021).

65. Quinton, R. J. et al. Whole-genome doubling confers unique genetic vulnerabilities on tumour cells. *Nature* **590**, 492–497 (2021).

66. Sievers, P. et al. CDKN2A/B homozygous deletion is associated with early recurrence in meningiomas. *Acta Neuropathol.* **140**, 409–413 (2020).

67. Merlo, A. et al. 5′ CpG island methylation is associated with transcriptional silencing of the tumour suppressor p16/CDKN2/MTS1 in human cancers. *Nat. Med.* **1**, 686–692 (1995).

68. Herman, J. G. et al. Distinct patterns of inactivation of p15INK4B and p16INK4A characterize the major types of hematological malignancies. *Cancer Res.* **57**, 837–841 (1997).

69. Levine, A. J., Jenkins, N. A. & Copeland, N. G. The roles of initiating truncal mutations in human cancers: the order of mutations and tumor cell type matters. *Cancer Cell* **35**, 10–15 (2019).

70. Tien, A.-C. et al. MNGI-01. A phase 0 trial of ribociclib in aggressive meningioma patients incorporating a tumor pharmacodynamic- and pharmacokinetic-guided expansion cohort. *Neuro Oncol.* **21**, vi139 (2019).

71. Bi, W. L. et al. Activity of PD-1 blockade with nivolumab among patients with recurrent atypical/anaplastic meningioma: phase II trial results. *Neuro. Oncol.* **24**, 101–113 (2021).

72. Pagès, F. et al. Immune infiltration in human tumors: a prognostic factor that should not be ignored. *Oncogene* **29**, 1093–1102 (2010).

Methods

This study complied with all relevant ethical regulations and was approved by the UCSF Institutional Review Board (13-12587, 17-22324, 17-23196 and 18-24633) and by The University of Hong Kong (HKU) Institutional Review Board (UW 07-273 and UW 21-112). As part of routine clinical practice at both institutions, all patients who were included in this study signed a waiver of informed consent to contribute deidentified data to research projects. Meningiomas and deidentified clinical information were transferred from HKU to UCSF in 2019 for analysis under protection of a Material Transfer Agreement that was certified by both institutions.

Meningiomas and clinical data. Meningioma samples for the discovery cohort were selected from the UCSF Brain Tumor Center Biorepository and Pathology Core in 2017, with an emphasis on high-grade meningiomas and low-grade meningiomas with long clinical follow-up. All WHO grade 2 and grade 3 meningiomas with available frozen samples were included. For WHO grade 1 meningiomas, frozen samples in the tissue bank were cross-referenced for clinical follow-up data from a retrospective institutional meningioma clinical outcomes database, and all cases with available frozen tissue and clinical follow-up greater than 10 years ($n = 40$) were included. To achieve a discovery cohort of 200 cases, additional WHO grade 1 meningiomas with available frozen tissue and the longest possible clinical follow-up (albeit less than 10 years, $n = 47$) were included. The electronic medical record was reviewed for all patients in late 2018, and paper charts were reviewed in early 2019 for patients treated before the advent of the electronic medical record. All available clinical pathology material was reviewed for diagnostic accuracy by a board-certified neuropathologist (D.A.S.). WHO grading was performed using contemporary criteria outlined in the WHO classification of tumors of the central nervous system[73]. Cases for which other tumors remained in the differential diagnosis (such as schwannoma or solitary fibrous tumor/hemangiopericytoma) were excluded. The validation cohort was comprised of 365 consecutive meningiomas from patients who were treated at HKU from 2000 to 2019 that had frozen tissue suitable for DNA methylation profiling. The medical record was reviewed for all patients in late 2019. For the discovery and validation cohorts, meningioma recurrence was defined as new radiographic tumor on magnetic resonance imaging after gross total resection, or enlargement/progression/growth of residual tumor on magnetic resonance imaging after subtotal resection. All magnetic resonance imaging studies in the discovery cohort were reviewed for accuracy and meningioma location by a board-certified radiologist with a Certificate of Added Qualification in Neuroradiology (J.E.V.-M.) (Supplementary Note). Nomograms integrating clinical and molecular features influencing meningioma outcomes were developed to guide clinical translation of meningioma DNA methylation groups (Supplementary Note).

DNA methylation profiling and analysis. DNA was extracted from all 565 meningiomas included in this study (Supplementary Note). Genomic DNA was processed on the Illumina Methylation EPIC Beadchip (WG-317-1003, Illumina) according to manufacturer's instructions at the Molecular Genomics Core at the University of Southern California. Downstream analysis was performed in R (v3.5.3 and v3.6.1) with SeSAMe (Bioconductor v3.10) (ref. [3]). Probes were filtered and analyzed using the standard SeSAMe preprocessing pipeline, including normal-exponential out-of-band background correction, nonlinear dye bias correction, P value with out-of-band array hybridization masking and β value calculation (β = methylated/[methylated + unmethylated]). A total of 272,041 probes were masked in at least one sample by the SeSAMe preprocessing pipeline, and 593,877 were retained for subsequent analysis.

Preprocessing and β value calculation were repeated using the minfi R package for comparison (Bioconductor v3.10) (ref. [9]), using functional normalization[74]. Probes were filtered based on the following criteria: (1) removal of probes containing common single-nucleotide polymorphisms within the targeted CpG sites or on an adjacent base pair ($n = 30,435$), (2) removal of probes targeting the X and Y chromosomes ($n = 19,298$), (3) removal of cross-reactive probes previously reported in the literature[75] ($n = 39,605$) and (4) removal of probes with a detection $P > 0.05$ in any samples ($n = 12,572$). A total of 763,949 probes were retained for analysis after minfi preprocessing, representing 31.4% more probes than were included for analysis using the SeSAMe preprocessing pipeline.

Principal-component (PC) analysis was performed independently on the β-methylation values from both the SeSAMe and minfi preprocessing pipelines in R using the base command 'prcomp' with the parameters 'center = TRUE, scale. = FALSE'. Variable probes were identified from the first three PCs, which were chosen for analysis in both preprocessing pipelines (SeSAMe and minfi). The elbow method identified three or four PCs as the optimal number, but PC4 was excluded from analysis, as it contributed to <5% of β value variance in both pipelines. In contrast, PC1–PC3 contributed to >5% of β value variance in both pipelines. The top 700 probes from PC1–PC3 (2,100 total probes) were selected for analysis by ranking the absolute gene loading score values within PCs. A cutoff of 700 probes for each PC was chosen based on the distribution of loading scores in an effort to balance signal and noise from probes minimally contributing to β value variance. Using 500, 1,000 or 15,00 probes only re-grouped 1%–4% of meningiomas, suggesting the precise number of probes across the top three

PCs did not affect unsupervised hierarchical clustering results. Duplicate probes were removed, and probes with the lowest gene loading scores were culled until 2,000 variable probes remained, which were used for unsupervised hierarchical clustering (Pearson correlation distance, Ward's method). Using all 2,094 unique probes did not affect unsupervised hierarchical clustering results, and using as few as 1,900 probes only reclustered 1% of meningiomas, suggesting the precise number of probes from the union set across the top three PCs did not affect unsupervised hierarchical clustering results.

Sampling distributions of DNA methylation group proportions were generated via bootstrapping, group number was investigated across PCs and DNA methylation preprocessing pipelines, and cell-type deconvolution was performed (Supplementary Note). In brief, the number of groups identified was independent of the number of PCs used for probe selection. SeSAMe consensus clustering clearly identified three clusters as the optimal number, whereas minfi consensus clustering was unable to discriminate between three and four clusters. Even within three groups, minfi reassigned 21% of meningiomas to different DNA methylation groups compared to the SeSAMe preprocessing pipeline.

CNV analysis. CNV profiles from DNA methylation data were generated with the 'cnSegmentation' command within the SeSAMe R package[76], using the 'EPIC.5.normal' dataset from the sesameData package as a copy-number-normal control. CNV profiles were generated independent of meningioma DNA methylation groups, and sample-level DNA methylation group identities were unblinded for integrated analyses in the context of other genetic data only after CNVs were defined. CNV intensity value distributions were manually inspected for local minima and maxima, and nadirs separating copy-number losses, gains and neutral events were identified. Segments with mean intensity values less than −0.1 were defined as copy-number losses, segments with mean intensity values greater than 0.15 were defined as copy-number gains, and segments with intensity values between −0.1 and 0.15 were defined as neutral copy-number events. Chromosome arms with at least 80% of their length meeting these criteria were considered losses or gains of the chromosomal arm, respectively. This analysis excluded sex chromosomes and the p arms of acrocentric chromosomes, which had insufficient methylation probes for robust CNV quantification (13p, 14p, 15p, 21p and 22p). The percentage of the genome with copy-number variation was determined by calculating the average number of segments per sample with mean intensity values less than −0.1 or greater than 0.15, weighted by segment length. Genome-wide CNV plots were generated using the R package karyoplotR (Bioconductor v3.10). CNVs of biological interest were verified using IGV. CNV definitions were validated using exome sequencing, the interdependence of meningioma CNVs and meningioma DNA methylation groups was tested, and the size and specificity of CNVs across meningioma DNA methylation groups was investigated (Supplementary Note).

RNA sequencing and analysis. RNA was extracted from the 200 meningioma discovery cohort (Supplementary Note). Library preparation was performed using the TruSeq RNA Library Prep Kit v2 (RS-122-2001, Illumina) and 50-bp single-end reads were sequenced on an Illumina HiSeq 4000 to a mean of 42 million reads per sample at the UCSF IHG Genomics Core. Quality control of FASTQ files was performed with FASTQC (v0.11.9). Reads were trimmed with Trimmomatic to remove Illumina adapter sequences[77], leading and trailing bases with quality scores below 20, and any bases that did not have an average quality score of 20 within a sliding window of four bases. Any reads shorter than 36 bases after trimming were removed. Reads were mapped to the human reference genome GRCh38 (ref. [78]) using HISAT2 (ref. [79]) (v2.1.0) with default parameters. For downstream expression analysis, exon-level count data were extracted from the mapped HISAT2 output using featureCounts (v2.0.1) (ref. [80]). Differential expression analysis and cell-type deconvolution were performed, hierarchical clustering using gene expression data was attempted and the specificity of FOXM1 signaling in Hypermitotic meningiomas was investigated (Supplementary Note).

Somatic short variant sequencing and analysis. A custom amplicon DNA sequencing panel was designed with 100% coverage of all coding exons of *NF2*, somatic short variants in *TRAF7* were identified from the RNA sequencing data, whole-exome sequencing data were analyzed, CLIA-certified exome sequencing was performed and analyzed, and major histocompatibility complex class I genotypes and mutant neoepitope peptides were inferred (Supplementary Note).

Immunoblotting, fractionation and immunoprecipitation. Immunoblots were used to assess protein expression in tissues, whole-cell lysates, subcellular fractions or immunoprecipitated samples (Supplementary Note). Immunoblot cell line samples were prepared by lysis in radioimmunoprecipitation assay (RIPA) buffer containing Complete-Mini EDTA-free protease inhibitor (11836170001, Sigma-Aldrich) and PhosSTOP phosphatase inhibitor (04906837001, Sigma-Aldrich), followed by boiling in Laemmli reducing buffer. Immunoblot meningioma samples were first mechanically lysed using a TissueLyser II (QIAGEN) according to the manufacturer's instructions then processed identically to cell line samples. Samples were separated on 4%–15% gradient TGX precast gels (4561086, Bio-Rad) and transferred onto nitrocellulose membranes (1620094, Bio-Rad). Membranes were blocked in 5% TBST-milk, incubated in primary

antibody, washed, and incubated in secondary antibodies. Membranes were subjected to immunoblot analysis using Pierce ECL (32209, Thermo Fischer Scientific) or SuperSignal West Femto (34095, Thermo Fischer Scientific) substrates. Primary antibodies were used against Merlin (ab88957, clone AF1G4, Abcam, 1:2,000), GAPDH (MA515738, clone GA1R, Thermo Fischer Scientific, 1:2,000), caspase-7 (9492, Cell Signaling Technology, 1:500), IRF8 (5628 S, clone D20D8, Cell Signaling Technology, 1:500), Tubulin (T5168, clone B-5-1-2, Sigma-Aldrich, 1:5,000), HH3 (702023, clone 17H2L9, Thermo Fisher Scientific, 1:1,000), FLAG (F1804, clone F1804, Sigma-Aldrich, 1:1,000), ARHGAP35 (2860, clone C59F7, Cell Signaling Technology, 1:1,000), FOXM1 (sc-376471, clone G-5, Santa Cruz Biotechnology, 1:500), pRB-S780 (8180 P, clone D59B7, Cell Signaling Technology, 1:1,000) or pRB-S807/811 (8516 P, clone D20B12, Cell Signaling Technology, 1:1,000). Secondary antibodies used were mouse (7076, Cell Signaling Technology, 1:2,000) or rabbit (7074, Cell Signaling Technology, 1:2,000).

Cell culture and organoids. HEK293T (CRL-3216, ATCC), BenMen[81], IOMM-Lee[23] or CH157-MN[26] cells were cultured in Dulbecco's modified Eagle medium (DMEM) (11960069, Life Technologies), supplemented with 10% fetal bovine serum (FBS) (16141, Life Technologies), 1× GlutaMAX (35050-061, Thermo Fischer Scientific) and 1× Penicillin/Streptomycin (15140122, Life Technologies). DI-98 or DI-134 cells[54] were cultured in DMEM supplemented with 7% FBS and 1× Penicillin/Streptomycin. M10G cells[22] were cultured in a 1:1 ratio of DMEM/F12 media (10565, Life Technologies) and Neurobasal media (21103, Life Technologies), supplemented with 5% FBS, B-27 supplement without vitamin A (12587, Life Technologies), N-2 supplement (17502, Life Technologies), 1× GlutaMAX (35050, Life Technologies), 1 mM NEAA (11140, Life Technologies), 100 U ml⁻¹ Anti-Anti (15240, Life Technologies), 20 ng ml⁻¹ epidermal growth factor (AF-100-15, Peprotech) and 20 ng ml⁻¹ fibroblast growth factor (AF-100-18B, Peprotech). MSC1 cells were cultured in the same conditions as M10G cells but supplemented with 15% FBS[22]. Meningioma cell lines were authenticated using DNA methylation profiling and CNV analyses to confirm concordance to tumors of origin, most recently in 2021. Nonmeningioma cell lines purchased from reputable commercial suppliers (HEK293T cells from ATCC) were not authenticated. Cell proliferation or apoptosis was investigated (Supplementary Note). Human cerebral organoids were created from astrocytes induced from pluripotent human stem cells and co-cultured with meningioma cells[22].

CRISPRi gene suppression. Lentiviral particles containing pMH0001 (ref. [82]) (UCOE-SFFV-dCas9-BFP-KRAB; 85969, Addgene) were produced by transfecting HEK293T cells with standard packaging vectors using the *Trans*IT-Lenti Transfection Reagent (6605, Mirus). M10G cells were stably transduced with lentiviral particles to generate M10G^dCas9-KRAB cells. Successfully transduced cells were isolated through selection of BFP-positive cells using fluorescence activated cell sorting on a Sony SH800.

Single-guide RNA (sgRNA) protospacer sequences were individually cloned into the pCRISPRia-v2 vector[83] (84832, Addgene), between the *Bst*XI and *Blp*I sites, by ligation. Each vector was verified by Sanger sequencing of the protospacer (Supplementary Table 14). Lentivirus was generated as described for each sgRNA expression vector. M10G^dCas9-KRAB cells were independently transduced with lentivirus from each sgRNA expression vector and selected to purity using 20 μg ml⁻¹ puromycin over 7 days.

shRNA gene suppression. Lentiviral particles containing pLKO.1 short hairpin RNA (shRNA) targeting control (RHS6848, Dharmacon) or *NF2* (RHS3979-201768826 or RHS3979-201768830) were generated by transfecting HEK293T cells with standard packaging vectors (psPAX2 and pMD2.9) and shRNA plasmids using *Trans*IT-Lenti Transfection Reagent. After 48 h virus production, viral particles were sterilized through a 0.45-μM filter and added to meningioma cells with polybrene 10 μg ml⁻¹ (TR-1003, MerkMillipore). A polyclonal population of shRNA-positive cells was selected using puromycin 2 μg ml⁻¹.

siRNA gene suppression. Small interfering RNA (siRNA) targeting the glucocorticoid receptor, NR3C1 (J-003424-10-0002), or control (D-001810-01-05) were purchased from Dharmacon. siRNA transfection was performed using Lipofectamine RNAiMax reagent (13778, Thermo Fischer Scientific). In brief, two cocktails containing either siRNA (25 nM) or Lipofectamine RNAiMax (3 μl) in 150 μl OptiMEM were made per transfection. Cocktails were incubated for 5 min before combination of the two solutions, followed by incubated for an additional 10 min before adding to cells for 15 h. The siRNA transfection was repeated after 48 h and expanded. Cells were collected 92 h after first siRNA transfection.

RNA extraction, cDNA synthesis and QPCR. RNA was extracted from cultured cells using the RNeasy Mini Kit (74106, QIAGEN) according to manufacturer's instructions. cDNA was synthesized from extracted RNA using the iScript cDNA Synthesis Kit (1708891, Bio-Rad). Real-time qPCR was performed using PowerUp SYBR Green Master Mix (A25918, Thermo Fisher Scientific) on a QuantStudio 6 Flex Real Time PCR system (Life Technologies) using forward and reverse primers (Supplementary Table 14). Real-time qPCR data were analyzed using the ΔΔCt method relative to *GAPDH* expression.

Immunofluorescence. Immunofluorescence of primary meningioma cells was performed on glass coverslips. Cells were fixed in 4% paraformaldehyde (15710, Electron Microscopy Sciences), blocked in 2.5% BSA (BP1600, Thermo Fischer Scientific) and 0.1% Triton-X100 (X100, Sigma) in phosphate-buffered saline (PBS) for 30 min at room temperature (14190, Gibco) and labeled with Ki-67 (ab15580, Abcam) primary antibodies at room temperature for 1 h. Cells were labeled with Alexa Fluor secondary antibodies and either Hoechst 33342 (H3570, Thermo Fisher Scientific) or DAPI (D3571, Thermo Fisher Scientific) to mark DNA for 1 h at room temperature and were mounted in ProLong Diamond Antifade Mountant (P36970, Thermo Fisher Scientific). For apoptosis assays, cells were washed in Annexin V binding buffer, stained with Annexin V for 15 min (550911, BD Bioscience), washed, labeled with DAPI to mark DNA for 1 h at room temperature and mounted in ProLong Diamond Antifade Mountant.

Immunofluorescence of human and xenograft meningiomas was performed on 10-μm cryosections of frozen tissue embedded in OCT Compound (Thermo Fisher Scientific). Slides with tissue were fixed in cold acetone for 10 min, air dried, washed in PBS, permeabilized with 0.3% Triton-X100 in PBS and washed again in PBS. Sections were blocked (2% BSA, 1% donkey serum and 0.1% Triton-X100 in PBS) for 30 min. Sections were labeled with either LYVE-1 (ab14917, Abcam, 1:1,000) or PROX1 (AF2727, R&D Systems, 1:1,000) primary antibodies at room temperature for 1 h. Slides were subsequently labeled with rabbit (A21206, Thermo Fischer Scientific, 1:1,000) and goat (A21469, Thermo Fischer Scientific 1:1,000) Alexa Fluor secondary antibodies and Hoechst 33342 to mark DNA for 1 h at room temperature and were mounted in ProLong Diamond Antifade Mountant.

Dual immunofluorescence of human meningiomas for FOXM1 and Ki-67 was performed on 5 μm formalin-fixed, paraffin-embedded (FFPE) human meningioma sections. Following antigen retrieval using CC1 for 32 min (950-124, Roche Diagnostics), sections were incubated and detected sequentially with rabbit monoclonal Ki-67 (90-4286, clone 30-9, Ventana, 1:4) and rabbit monoclonal FOXM1 primary antibodies (ab207298, clone EPR17379, Abcam, 1:600). Each primary antibody incubation was 32 min, and single stained controls were used to verify specificity. FOXM1 labeling index was quantified based on the total amount of nuclei with strong immunoreactivity for FOXM1 within a ×200 field. Ki-67 labeling index was quantified based on the total amount of nuclei with strong immunoreactivity for Ki-67 within a ×200 field. The labeling index for both FOXM1 and Ki-67 was averaged across two ×200 fields for each meningioma.

Histology and immunohistochemistry. Deparaffinization and rehydration of 5 μm FFPE human and mouse meningioma tissue sections and hematoxylin and eosin staining were performed using standard procedures. Immunostaining was performed on an automated Ventana Discovery Ultra staining system. Immunohistochemistry was performed on 5 μm FFPE meningioma xenograft sections using rabbit monoclonal Ki-67 (790-4286, clone 30-9, Ventana, 1:6) with primary antibody incubation for 16 min following CC1 antigen retrieval for 8 min, rabbit monoclonal cleaved caspase-3 (9664, clone 5A1E, Cell Signaling Technology, 1:2,000) with primary antibody incubation for 32 min at 37 °C following CC1 antigen retrieval for 8 min or rabbit polyclonal CD3 (A0452, Agilent Technologies, 1:200) with primary antibody incubation for 32 min at 37 °C following CC1 antigen retrieval for 8 min. Tumors were scored CD3 positive if multiple aggregates of CD3-positive lymphocytes were identified and were otherwise scored as CD3 negative.

Microscopy. Fluorescence microscopy was performed on a LSM 800 confocal laser scanning microscope with a PlanApo ×20 air objective (Zeiss). Images were processed and quantified from representative regions of each tumor or coverslip using ImageJ (v.2.1.0). Histologic and immunohistochemical features were evaluated using light microscopy on an BX43 microscope with standard objectives (Olympus). Images were obtained and analyzed using the Olympus cellSens Standard Imaging Software package.

Proteomic proximity-labeling mass spectrometry. M10G cells encoding pLV-APEX2-Merlin wild-type and L46R-mutant constructs were seeded onto 5 × 15 cm plates. For APEX labelling, cells were treated with 0.5 μM Biotin-phenol (BT1015, Berry & Associates) and returned to 37 °C, 5% CO₂ for 30 min. After 24 h, Merlin protein expression was induced with 0.1 μg ml⁻¹ doxycycline. Biotin-treated cells were subject to free radical formation by adding media containing 1 mM H₂O₂ to cells for exactly 30 s, on ice. Immediately, H₂O₂ media was aspirated and the reaction was quenched (10 mM sodium ascorbate, 1 mM azide and 5 mM Trolox), and cells were pelleted for biotin/streptavidin precipitation, reversed-phase gradient extraction and mass spectrometry (Supplementary Note).

Gene overexpression. For transient overexpression of FOXM1 or USF1, M10G cells were transfected with pCMV6-FOXM1 (RC202246, OriGene) or pCMV6-USF1 (RC204915, OriGene) plasmids at a ratio of 1 μg DNA to 2 μl FuGENE transfection reagent (E2311, Promega). Cells were collected 48 h after transfection for RNA extraction. For stable overexpression, USF1 was cloned from pCMV6-USF1 into the pLVX-IRES-puro vector using restriction digest and ligation. Lentivirus was generated and introduced onto CH-157MN cells and stable polyclonal cell lines were generated using antibiotic selection as described above.

Mice. This study was approved by the UCSF Institutional Animal Care and Use Committee (AN174769), and all experiments complied with relevant ethical regulations. Xenograft experiments were performed by implanting 3 million CH-157MN cells into the flank of 5- to 6-week-old female NU/NU mice (Harlan Sprague Dawley). To induce Merlin expression in meningiomas in vivo, mice harboring CH-157MN cells encoding pLV.APEX2-Merlin were treated with doxycycline 200 μg ml^{-1} ($n=3$) (D9891, Sigma-Aldrich) or vehicle ($n=3$) 14 days after implantation. After 7 days of treatment, 2 Gy ionizing radiation per day was delivered using a Precision X-RAD 320 Cabinet Irradiation, with normal operating settings, on each of 2 successive days. Tumors were collected 24 h after the second dose of ionizing radiation for immunoblotting and immunohistochemistry. For preclinical pharmacologic experiments, animals in the treatment arm ($n=7$) were gavaged with 100 μg g^{-1} abemaciclib in 0.5% methylcellulose vehicle daily starting 12 days after injection, until protocol-defined endpoints. Animals in the vehicle arm ($n=13$) were gavaged at the same frequency for the same duration with 0.5% methylcellulose. For Kaplan–Meier survival analysis, events were recorded when tumors reached the protocol-defined size of 2,000 mm^3.

Single-cell isolation and RNA sequencing. Fresh human meningioma ($n=8$) and dura ($n=2$) samples were acquired from the operating room and transported to the laboratory in PBS at 4 °C. These samples were not part of the discovery or validation cohorts, but all patients signed a waiver of informed consent to contribute deidentified data to research projects in compliance with all relevant ethical regulations under the supervision of the UCSF Institutional Review Board, as described above. Tissue samples were minced with sterile #10 scalpels (4-410, Integra LifeSciences) and incubated at 37 °C in a Collagenase Type 7 solution (LS005332, Worthington) until digested (30–60 min). Collagenase was used at a concentration of 0.1 mg ml^{-1} for tumor and brain–tumor interface samples and at a concentration of 0.2 mg ml^{-1} for dura samples. Samples were incubated in Trypsin-EDTA 0.25% (25200056, Thermo Fisher Scientific) at 37 °C for 5 min and in 1× RBC lysis buffer (00-4300-54, eBioscience) at room temperature for 10 min. Finally, samples were sequentially filtered through 70-μM and 40-μM cell strainers (352350 and 352340, Corning) to generate single-cell suspensions.

Single-cell suspensions were processed for single-cell RNA sequencing using a 10x Chromium controller, and libraries were generated using the Chromium Single Cell 3' Library & Gel Bead Kit v3 on a 10x Chromium controller using the manufacturer recommended default protocol and settings (1000121, 10x Genomics), at a target cell recovery of 5,000 cells per sample. Libraries were sequenced on an Illumina NovaSeq 6000, targeting >50,000 reads per cell, at the UCSF Center for Advanced Technology.

Single-cell RNA sequencing analysis. Library demultiplexing, read alignment to the GRCh38 human reference genome, identification of empty droplets, and UMI quantification was performed using CellRanger version 3.0.2 (https://github.com/10xGenomics/cellranger). Cells with greater than 500 unique genes, less than 10,000 unique genes and less than 20% of reads attributed to mitochondrial transcripts were retained. Single-cell UMI count data were preprocessed in R 1 with the Seurat[84,85] package (v3.0.1) using the sctransform[86] workflow, with scaling based on regression of UMI count and percentage of reads attributed to mitochondrial genes per cell. Dimensionality reduction was performed using PC analysis, and PCs were corrected for batch effects using Harmony (v0.1) (ref. [87]). Uniform manifold approximation and projection was performed on the reduction data with a minimum distance metric of 0.2, and Louvain clustering was performed using a resolution of 0.4. Marker identification and differential gene expression was performed in Seurat using a minimum fraction of detection of 0.75 and a minimum log-fold change of 0.5. CNVs were defined in single cells, cell types were defined using marker genes and cell cycle phases and reference transcriptomic signatures were defined (Supplementary Note).

ChIP sequencing and enhancer/superenhancer analysis. H3K27ac ChIP sequencing data were derived from 25 previously reported meningiomas[54] (3 Merlin-intact, 7 Immune-enriched and 15 Hypermitotic), and enhancer or superenhancer analyses were performed (Supplementary Note). USF1 enrichment at the *CDK6* promoter was investigated using ChIP qPCR (Supplementary Note).

Statistics. All experiments were performed with independent biological replicates and repeated, and statistics were derived from biological replicates. Biological replicates are indicated in each panel or figure legend. No statistical methods were used to predetermine sample sizes, but our discovery and validation cohort sizes are similar or larger to those reported in previous publications[4,5,8]. Data distribution was assumed to be normal, but this was not formally tested. Investigators were blinded to conditions during clinical data collection and analysis of mechanistic or functional studies. Bioinformatic analyses were performed blind to clinical features, outcomes or molecular characteristics. The clinical samples used in this study were retrospective and nonrandomized with no intervention, and all samples were interrogated equally. Thus, controlling for covariates among clinical samples is not relevant. Cells, organoids and animals were randomized to experimental conditions. No clinical, molecular, cellular or animal data points were excluded from the analyses. Unless specified otherwise, lines represent means, and error

bars represent standard error of the means. Results were compared using log-rank tests, Student's *t*-tests, ANOVA, chi-squared tests, Fisher's exact tests and Wald tests, which are indicated in Methods and figure legends alongside approaches used to adjust for multiple comparisons. Results comparisons in Supplementary tables were performed using Wald tests (Supplementary Table 6, 9 and 11, two sided Benjamin–Hochberg adjustment for multiple comparisons) or Wilcoxon rank-sum tests (Supplementary Table 10, two-sided Bonferroni adjustment for multiple comparisons). In general, statistical significance is shown by asterisks (*$P \le 0.05$, **$P \le 0.01$ or ***$P \le 0.0001$), but exact P values are provided in the figure legends.

Reporting Summary. Further information on research design is available in the Nature Research Reporting Summary linked to this article.

Data availability

DNA methylation ($n=565$), RNA sequencing ($n=185$), and single-cell RNA sequencing data ($n=8$ meningioma samples, $n=2$ dura samples) of new samples reported in this manuscript have been deposited in the NCBI Gene Expression Omnibus under the accession GSE183656. Additional RNA sequencing data from previously reported meningiomas ($n=15$) from the discovery cohort are available under the accession GSE101638. Whole-exome sequencing, ChIP sequencing, and additional DNA methylation profiling data incorporated into this study were derived from previously reported and deposited meningiomas in GSE101638, GSE139652. The publicly available GRCh38 (hg38, https://www.ncbi.nlm.nih.gov/assembly/GCF_000001405.39/) and GRCh37.p13 datasets (hg19, https://www.ncbi.nlm.nih.gov/assembly/GCF_000001405.25/) were used in this study. Source data are provided with this paper.

Code availability

The open-source software, tools, and packages used for data analysis in this study, as well as the version of each program, were ImageJ (v2.1.0), R (v3.5.3 and v3.6.1), FASTQC (v0.11.9), HISAT2 (v2.1.0), featureCounts (v2.0.1), Seurat R package (v3.0.1), Harmony R package (v0.1), caret R package (v6.0-90), Rtsne R package (v0.15), PAMES R package (v2.6.2), CONICSmat R package (v1.0), DeepTools (v3.1.2), survival R package (v3.2-13), survAUC R package (v1.0-5), rms R package (v6.2-0), rpart R package (v4.1.16), DynNom R package (v5.0.1), DESeq2 (Bioconductor v3.10), SeSAMe (Bioconductor v3.10), minfi (Bioconductor v3.10), karyoplotR (Bioconductor v3.10), ConsensusClusterPlus (Bioconductor v3.10), and DiffBind (Bioconductor v3.10). No software was used for data collection. A methylation profile multi-class support vector machine (SVM) classifier was generated using the caret R package[88], and was deposited in the GitHub repository abrarc/meningioma-svm (ref. [89]). In brief, a linear kernel SVM was constructed using training data comprising 75% of randomly selected samples from the discovery cohort ($n=150$) with 10-fold cross validation. 2,000 probes from each preprocessing pipeline were used as variables. The remaining 25% of samples from the discover cohort ($n=50$) were used to test the model, which performed with 97.9% accuracy when classifying samples into three SeSAMe groups (95% CI 89.2-99.9%, $P < 2.2 \times 10^{-16}$). SVM classifiers for 3, 4, 5, or 6 minfi groups were generated using the same approach and performed with 91.8% (95% CI 80.4%-97.7%, $P = 4.69 \times 10^{-9}$), 91.8% (95% CI 80.4%-97.7%, $P = 9.58 \times 10^{-16}$), 93.8% (95% CI 82.8%–98.7%, $P = 2.98 \times 10^{-16}$), and 93.6% (95% CI 82.5%-98.7%, $P < 2.2 \times 10^{-16}$) accuracy, respectively. SVM classification and K-means consensus clustering of the validation cohort was performed with the same parameters as for the discovery cohort using the same probes in the validation cohort that were identified from the discovery cohort.

References

73. Louis, D., Ohgaki, H., Wiestler, O. & Cavenee, W. *WHO Classification of Tumours of the Central Nervous System* (IARC Publications, 2016).
74. Fortin, J.-P. et al. Functional normalization of 450k methylation array data improves replication in large cancer studies. *Genome Biol.* **15**, 503 (2014).
75. Pidsley, R. et al. Critical evaluation of the Illumina MethylationEPIC BeadChip microarray for whole-genome DNA methylation profiling. *Genome Biol.* **17**, 208 (2016).
76. Capper, D. et al. DNA methylation-based classification of central nervous system tumours. *Nature* **555**, 469–474 (2018).
77. Bolger, A. M., Lohse, M. & Usadel, B. Trimmomatic: a flexible trimmer for Illumina sequence data. *Bioinformatics* **30**, 2114–2120 (2014).
78. Schneider, V. A. et al. Evaluation of GRCh38 and de novo haploid genome assemblies demonstrates the enduring quality of the reference assembly. *Genome Res.* **27**, 849–864 (2017).
79. Kim, D., Paggi, J. M., Park, C., Bennett, C. & Salzberg, S. L. Graph-based genome alignment and genotyping with HISAT2 and HISAT-genotype. *Nat. Biotechnol.* **37**, 907–915 (2019).
80. Liao, Y., Smyth, G. K. & Shi, W. featureCounts: an efficient general purpose program for assigning sequence reads to genomic features. *Bioinformatics* **30**, 923–930 (2014).
81. Püttmann, S. et al. Establishment of a benign meningioma cell line by hTERT-mediated immortalization. *Lab. Invest.* **85**, 1163 (2005).

82. Adamson, B. et al. A multiplexed single-cell CRISPR screening platform enables systematic dissection of the unfolded protein response. *Cell* **167**, 1867–1882 (2016).

83. Horlbeck, M. A. et al. Compact and highly active next-generation libraries for CRISPR-mediated gene repression and activation. *eLife* **5**, e19760 (2016).

84. Butler, A., Hoffman, P., Smibert, P., Papalexi, E. & Satija, R. Integrating single-cell transcriptomic data across different conditions, technologies, and species. *Nat. Biotechnol.* **36**, 411–420 (2018).

85. Stuart, T. et al. Comprehensive integration of single-cell data. *Cell* **177**, 1888–1902 (2019).

86. Hafemeister, C. & Satija, R. Normalization and variance stabilization of single-cell RNA-seq data using regularized negative binomial regression. *Genome Biol.* **20**, 296 (2019).

87. Korsunsky, I. et al. Fast, sensitive and accurate integration of single-cell data with Harmony. *Nat. Methods* **16**, 1289–1296 (2019).

88. James, G., Witten, D., Hastie, T. & Tibshirani, R. *An Introduction to Statistical Learning: with Applications in R* (Springer, 2021).

89. Choudhury, A. abrarc/meningioma-svm. *Zenodo* https://doi.org/10.5281/zenodo.6353877 (2022).

Author contributions

All authors made substantial contributions to the conception or design of the study; the acquisition, analysis, or interpretation of data; or drafting or revising the manuscript. All authors approved the manuscript. All authors agree to be personally accountable for individual contributions and to ensure that questions related to the accuracy or integrity of any part of the work are appropriately investigated and resolved and the resolution documented in the literature. A.C. designed, performed and analyzed most of the experiments and bioinformatic analyses. S.T.M. extracted nucleic acids from all meningiomas, collected clinical data and was involved in the inception, execution and supervision of all aspects of the study. M.S.S. assembled clinical data for the discovery cohort. C.D.E. performed biochemical and apoptosis assays and supervised T.J.C.-C. to perform APEX reactions. B.C.P. analyzed ChIP sequencing data and performed ChIP qPCR experiments with Z.Q. under J.N.R.'s supervision. W.C.C. developed nomograms and performed CNV recursive partitioning analysis. M.A.C. performed immunofluorescence and mouse experiments. K.S. performed organoid experiments. C.H.G.L. analyzed meningioma histology under D.A.S.'s and A.P.'s supervision. H.N.V. and S.J.L. provided bioinformatic guidance. J.E.V.-M. analyzed magnetic resonance imaging studies to define meningioma locations. T.-C.L., J.K.-S.P., L.-F.L., G.K.-K.L. and J.W.C. assembled clinical data and meningiomas for the validation cohort. D.L.S. performed proteomic proximity-label mass spectrometry under N.J.K.'s supervision. M.Y.Z. and M.V.M. performed HLA genotyping and neoantigen prediction under J.F.C.'s supervision. N.A.O.B. treated meningioma patients with CDK4/6 inhibitors. J.J.P. performed immunohistochemistry. S.E.B., J.S., N.B., P.K.S., M.S.B. and M.W.M. provided clinical data and meningiomas for the discovery cohort. D.R.R. conceived, designed and supervised the study.

Competing interests

The authors declare no competing interests.

Additional information

Extended data is available for this paper at https://doi.org/10.1038/s41588-022-01061-8.

Supplementary information The online version contains supplementary material available at https://doi.org/10.1038/s41588-022-01061-8.

Correspondence and requests for materials should be addressed to Stephen T. Magill, Jeremy N. Rich or David R. Raleigh.

Peer review information *Nature Genetics* thanks Roel Verhaak and the other, anonymous, reviewer(s) for their contribution to the peer review of this work. Peer reviewer reports are available.

**Reprints and permissions information** is available at www.nature.com/reprints.
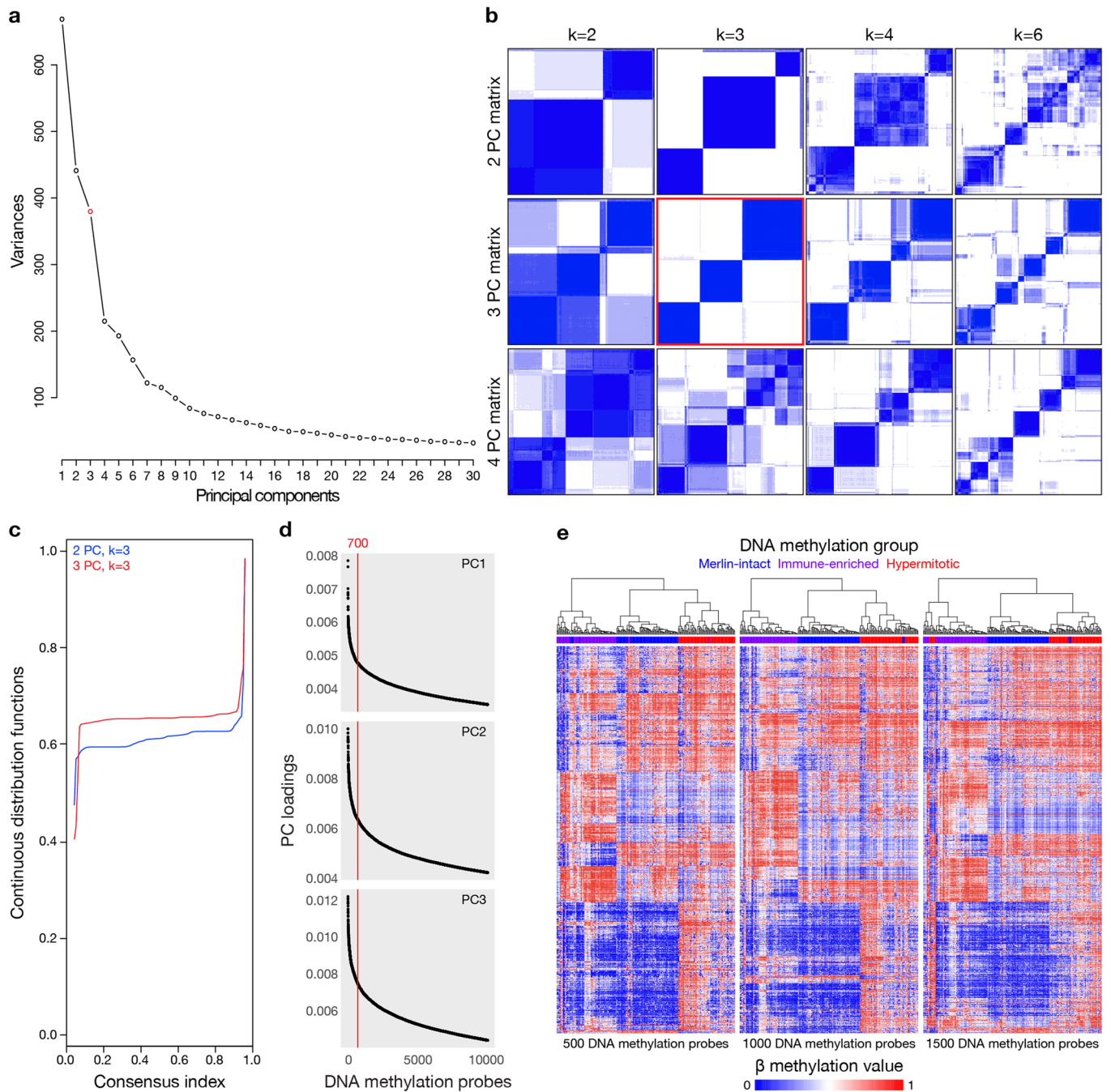
Extended Data Fig. 1 | DNA methylation analysis using SeSAMe to control for the influence of CNVs on β values identifies three groups of meningiomas. a, Scree/elbow plot of principal component analysis (PCA) of meningioma DNA methylation profiles suggesting differentially methylated DNA probes from the top 3 to 4 principal components (PCs) provide the most information in the discovery cohort (n=200). **b**, K-means consensus clustering of meningioma DNA methylation profiles from the discovery cohort (n=200) using differentially methylated DNA probes from the top 2-4 PCs across k=2-7 groups, suggesting 3 PCs and k=3 groups are optimal. **c**, Continuous distribution functions from K-means consensus clustering of meningiomas from the discovery cohort (n=200) using differentially methylated DNA probes from the top 2 or 3 PCs across k=3 groups, validating 3 PCs as the optimal number (p<2.2×10⁻¹⁶, Kolmogorov-Smirnov test). **d**, Distribution of absolute DNA methylation probe loadings across the top 3 PCs from the discovery cohort (n=200) for the top 10,000 probes for each PC. Loading distribution plots for each PC were similar, and the top 700 probes for each PC were selected using the elbow method for meningioma clustering. **e**, Unsupervised hierarchical clustering of meningiomas from the discovery cohort (n=200) using 500, 1000, or 1500 differentially methylated DNA probes from each PC demonstrating the precise number of probes from each PC does not significantly influence meningioma DNA methylation grouping. In comparison to Fig. 1b, altering the number of probes for meningioma DNA methylation grouping only altered assignments for 3-9 meningiomas (1-4%). Merlin-intact (blue), Immune-enriched (purple), and Hypermitotic (red) DNA methylation group assignments are from Fig. 1b.
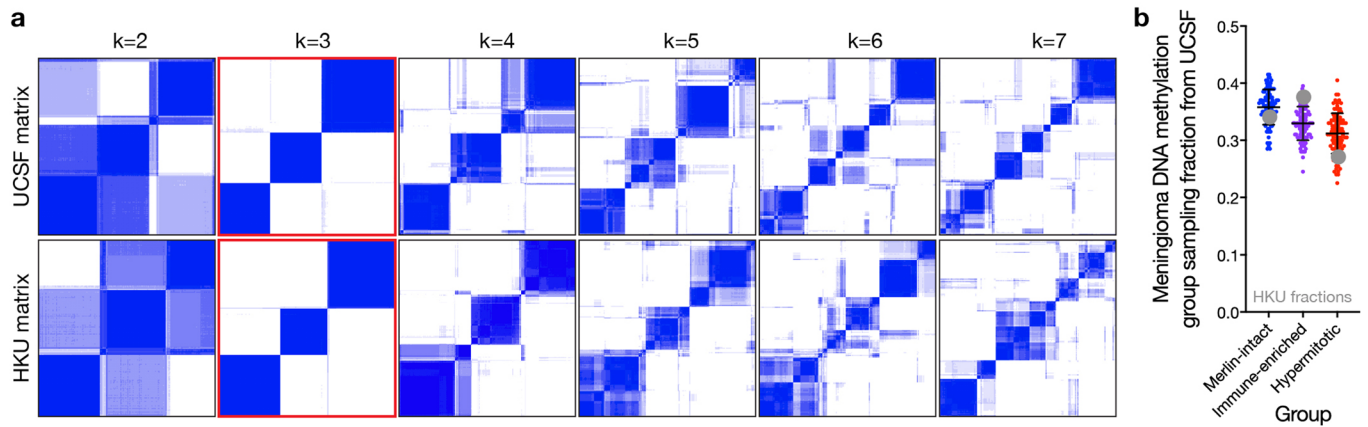
Extended Data Fig. 2 | Independent validation of three meningioma DNA methylation groups. a, K-means consensus clustering of meningioma DNA methylation profiles from the discovery (n=200, UCSF) and validation (n=365, HKU) cohorts. **b**, Sampling distributions of DNA methylation group fractions from the discovery cohort (n=100 per DNA methylation group), with the observed DNA methylation group fractions from the validation cohort denoted in grey. Lines represent means, and error bars represent standard deviations. The observed fractions of each DNA methylation group from the validation cohort fall within the sampling distributions from the discovery cohort.
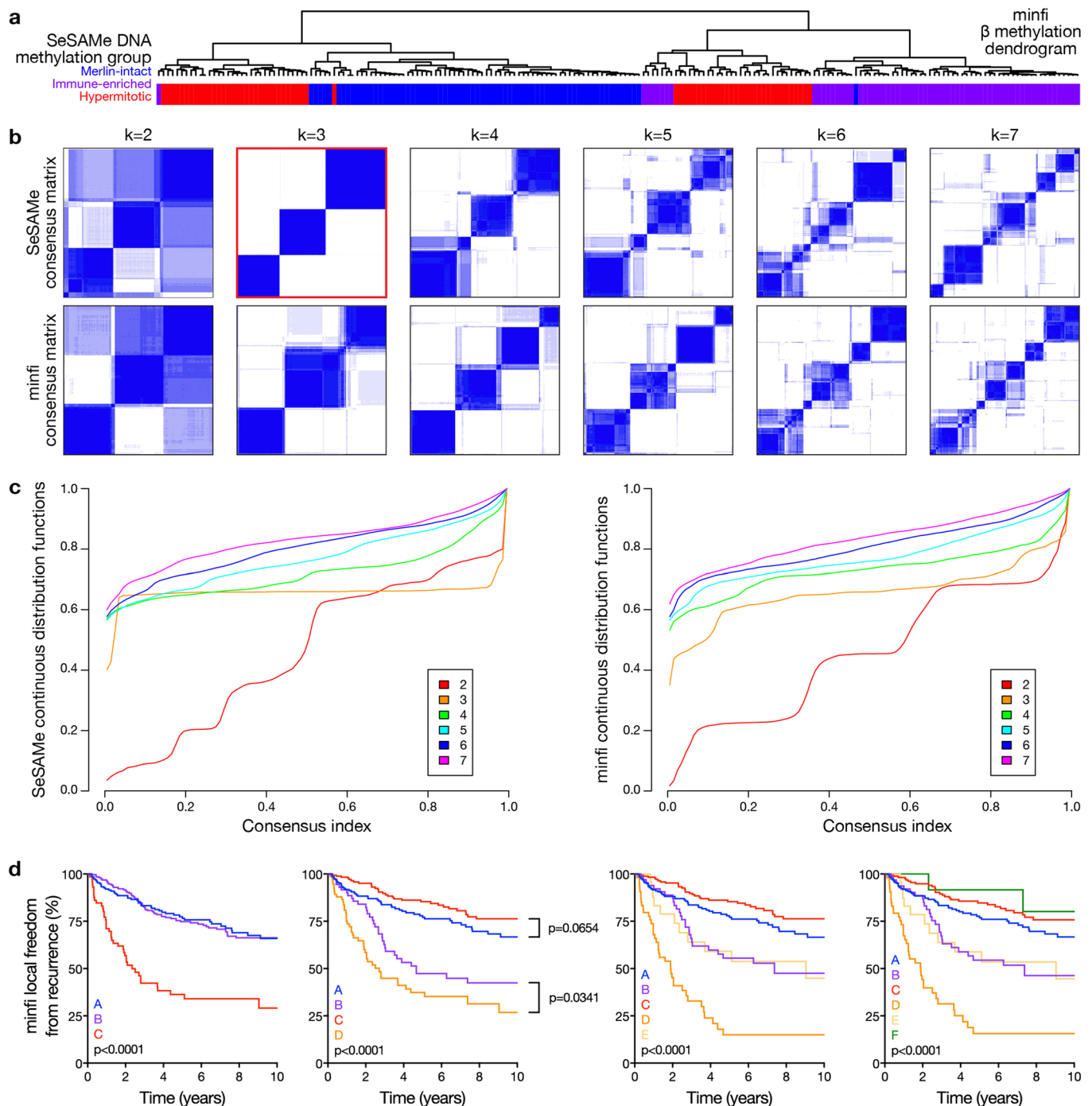
Extended Data Fig. 3 | Meningioma DNA methylation grouping using SeSAMe to control for the influence of CNVs on β values compared to approaches that do not control for the influence of CNVs on β values. a, Unsupervised hierarchical clustering of meningiomas from the discovery cohort (n=200) using 2,000 differentially methylated DNA probes from the minfi preprocessing pipeline, which does not control for the influence of CNVs on β values. SeSAME meningioma DNA methylation groups (21% altered by minfi) are shown beneath the vertical dendrogram. **b**, K-means consensus clustering of meningiomas from the discovery and validation cohorts (n=565) using differentially methylated DNA probes and β values from SeSAMe or minfi. SeSAMe consensus clustering identifies 3 groups as the optimal number, but minfi consensus clustering is unable to discriminate between 3 and 4 clusters. **c**, Continuous distribution functions (CDFs) from K-means consensus clustering of meningiomas from the discovery and validation cohorts (n=565) using differentially methylated DNA probes and β values from SeSAMe or minfi. SeSAMe CDFs validated 3 groups as the optimal number, which was quantitatively different from 3 minfi groups (p=1.341×10^{-4}) or 4 minfi groups (p<2.2×10^{-6}) (Kolmogorov-Smirnov test). **d**, Kaplan–Meier curves for meningioma local freedom from recurrence (n=565) across minfi DNA methylation groups fails to identify a grouping scheme with non-redundant differences in clinical outcomes, in contrast to SeSAMe DNA methylation groups (Fig. 1c) (Log-rank tests). minfi meningioma DNA methylation grouping schemed comprised of 3, 4, 5, or 6 groups are designated by letters A-C, A-D, A-E, or A-F, respectively.
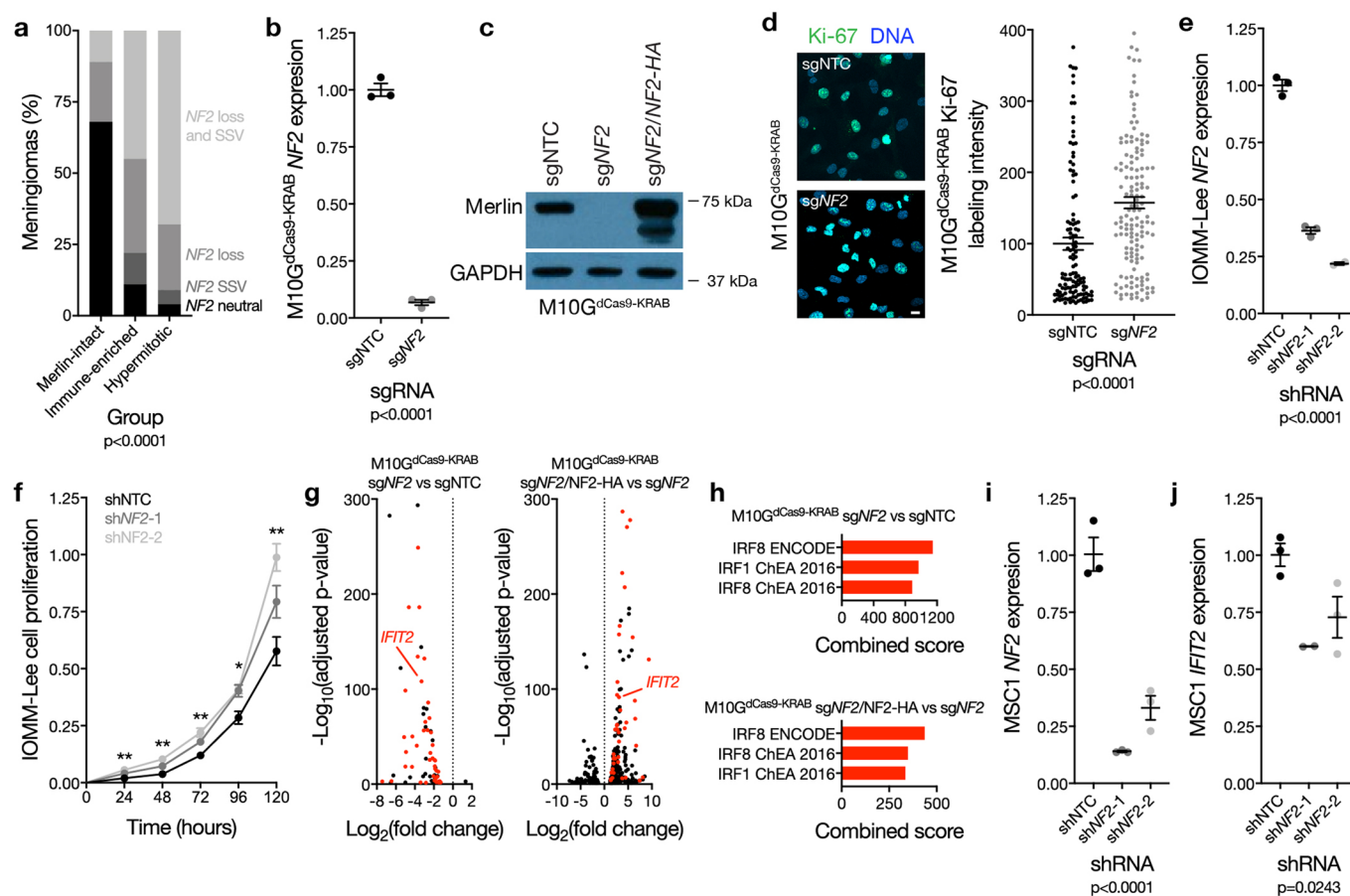
Extended Data Fig. 4 | Mechanisms of *NF2*/Merlin tumor suppression in meningioma cells. a, Meningioma *NF2* copy-number deletions containing the entire locus and targeted sequencing of somatic short variants (SSV, n = 65) across DNA methylation groups (Chi-squared test, two-sided). **b**, QPCR for *NF2* in M10G$^{dCas9-KRAB}$ cells expressing a non-targeting control single-guide RNA (sgNTC) or a single-guide RNA suppressing *NF2* (sg*NF2*). 3 biological replicates per condition (Student's t test, one sided). **c**, Immunoblot for Merlin or GAPDH in M10G$^{dCas9-KRAB}$ cells expressing sgNTC, sg*NF2*, or sg*NF2* with *NF2* rescue (sg*NF2* + *NF2*^{HA}). **d**, Confocal immunofluorescence microscopy and quantification of Ki-67 in M10G$^{dCas9-KRAB}$ cells from **b**. DNA is marked with Hoechst 33342. Scale bar 10 μM. From left to right, 123 or 145 cells are shown (Student's t test, one sided). **e**, QPCR for *NF2* in IOMM-Lee cells stably expressing a non-targeting control shRNA (shNTC) or shRNAs suppressing *NF2* (sh*NF2*-1 or sh*NF2*-2). From left to right, 3, 3, or 2 biological replicates are shown (ANOVA, one sided). **f**, MTT cell proliferation of IOMM-Lee cells from **e**, normalized to shNTC at 120 h. 4 biological replicates per condition per timepoint. *p = 0.0101, **p≤0.01 (ANOVA, one sided). **g**, Volcano plots of relative gene expression from RNA sequencing of M10G$^{dCas9-KRAB}$ cells in **c**. Interferon-regulated genes (including *IFIT2*, validated in **j**) are marked in red. **h**, Gene ontology analysis of differentially expressed genes from RNA sequencing of M10G$^{dCas9-KRAB}$ cells in **g**. **i**, QPCR for *NF2* in MSC1 cells stably expressing shNTC, sh*NF2*-1, or sh*NF2*-2. 3 biological replicates per condition (ANOVA, one sided). **j**, QPCR for the IRF target gene *IFIT2* in MSC1 cells from **i**. From left to right, 3, 2, or 3 biological replicates are shown (ANOVA, one sided). Lines represent means, and error bars represent standard error of the means.
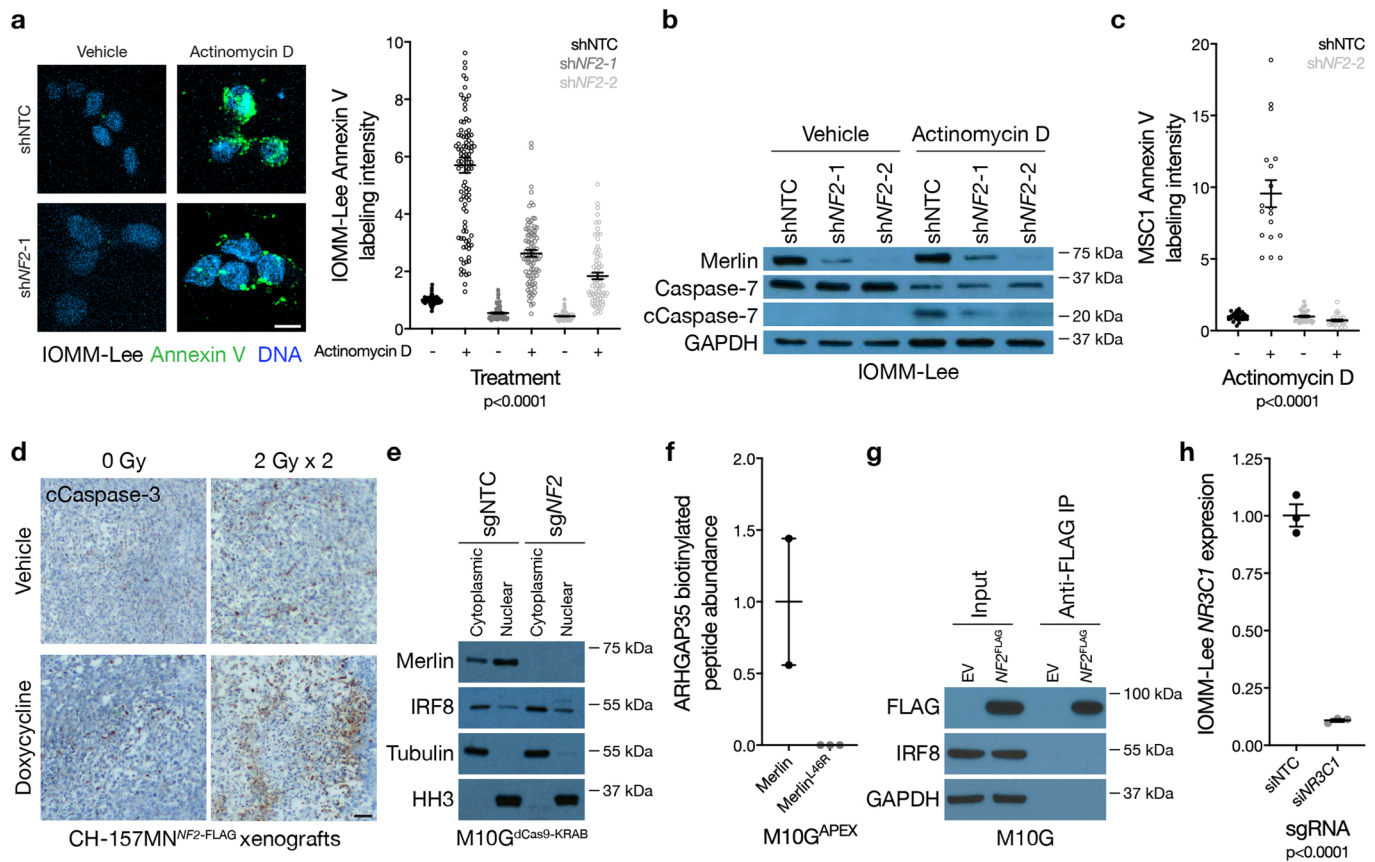
Extended Data Fig. 5 | *NF2*/Merlin drives meningioma apoptosis. a, Confocal microscopy and quantification of Annexin V in IOMM-Lee cells from Extended Data Fig. 4e treated with actinomycin D or vehicle control for 24 h. DNA is marked with DAPI. Scale bar 10 μM. From left to right, 96, 101, 95, 90, 98, or 75 cells are shown (ANOVA, one sided). **b**, Immunoblot Merlin, Caspase-7, cleaved Caspase-7 (cCaspase-7), or GAPDH in IOMM-Lee cells from **a**. **c**, Quantification of Annexin V confocal microscopy in MSC1 cells stably expressing sgNTC or sg*NF2*-2. Cells were treated as in **a**. From left to right, 29, 19, 40, or 30 cells are shown (ANOVA, one sided). **d**, Representative images of cleaved Caspase-3 (cCaspase-3) immunohistochemistry from CH-157MN xenografts stably expressing doxycycline-inducible Merlin encoding a FLAG tag (*NF2*-FLAG) in NU/NU mice after 7 days of doxycycline (n = 6) or vehicle treatment (n = 6), and 24 h after 4 Gy ionizing radiation (n = 6) or control treatment (n = 6). Scale bar 100 μM. **e**, Immunoblot for Merlin, IRF8, Tubulin, or Histone H3 (HH3) in cytoplasmic or nuclear fractions of M10G^dCas9-KRAB cells from Extended Data Fig. 4b. **f**, Normalized proteomic proximity-labeling mass spectrometry from M10G cells stably expressing Merlin constructs with APEX tags. From left to right, 2 or 3 biological replicates are shown. **g**, Immunoblot IRF8 or FLAG after FLAG immunoprecipitation from M10G cells stably expressing Merlin encoding a FLAG tag (*NF2*^FLAG). EV, empty vector. **h**, QPCR for the glucocorticoid receptor (*NR3C1*) in IOMM-Lee cells expressing a non-targeting control siRNA (siNTC) or siRNAs suppressing *NR3C1* (si*NR3C1*). 3 biological replicates per condition (Student's t test, one sided). Lines represent means, and error bars represent standard error of the means.
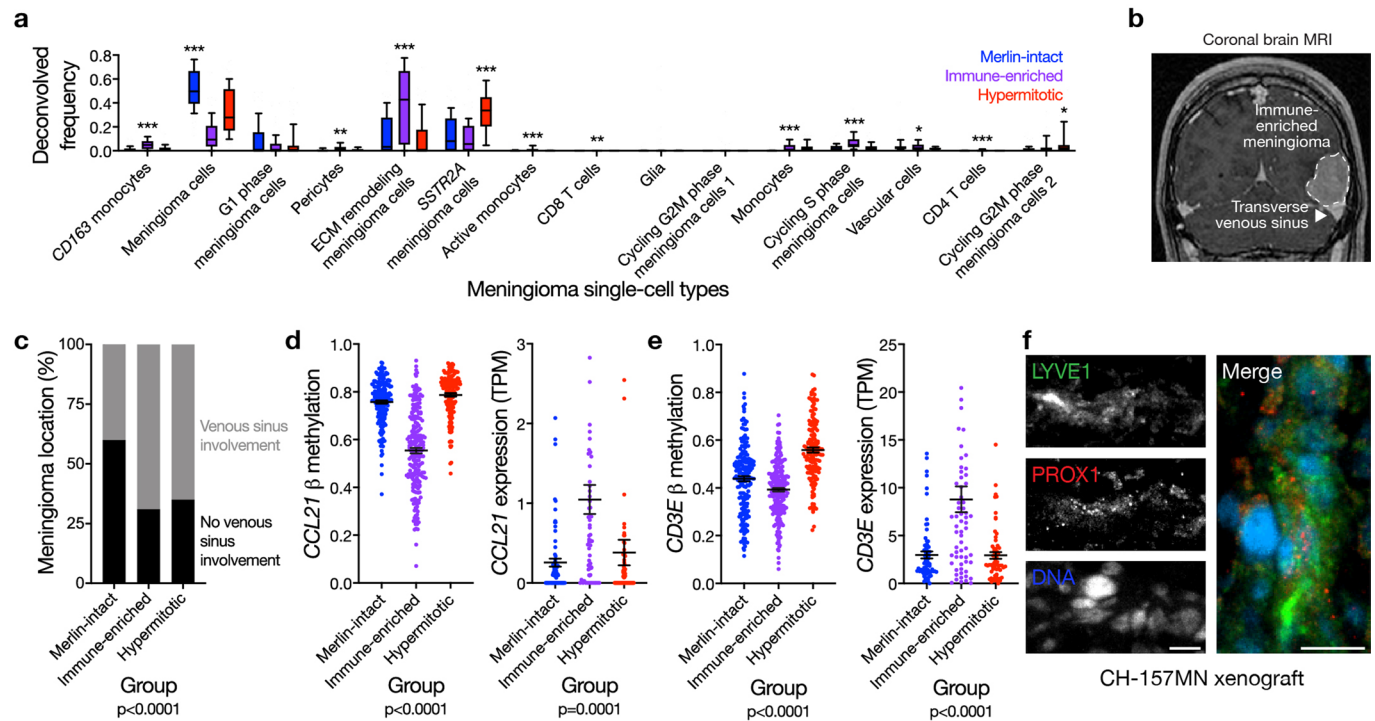
Extended Data Fig. 6 | Lymphatic vessels underlie meningioma immune infiltration. a, Fraction of meningioma samples (n = 200) classified meningioma single-cell types across DNA methylation groups, based on single-cell reference transcriptomes. Lines represent means, boxes represent inner quartile ranges, and error bars represent 10th-90th percentiles (ANOVA, one sided). **b**, **c**, Meningioma location on preoperative magnetic resonance imaging (n = 169) across DNA methylation groups (Chi-squared test, two-sided). Representative magnetic resonance image shown. **d**, Meningioma DNA methylation (n = 565) of *CCL21* (cg27443224) and TPM expression (n = 200) of *CCL21* across DNA methylation groups (ANOVA, one sided). **e**, Meningioma DNA methylation (n = 565) of *CD3E* (cg08956138) and TPM expression (n = 200) of *CD3E* across DNA methylation groups (ANOVA, one sided). **f**, Representative image of LYVE1 and PROX1 confocal immunofluorescence microscopy in CH157-MN xenografts in NU/NU mice (n = 3). DNA is marked with Hoechst 33342. Scale bars 10 μM. Lines represent means, and error bars represent standard error of the means. *p≤0.05, **p≤0.01, ***p≤0.0001.
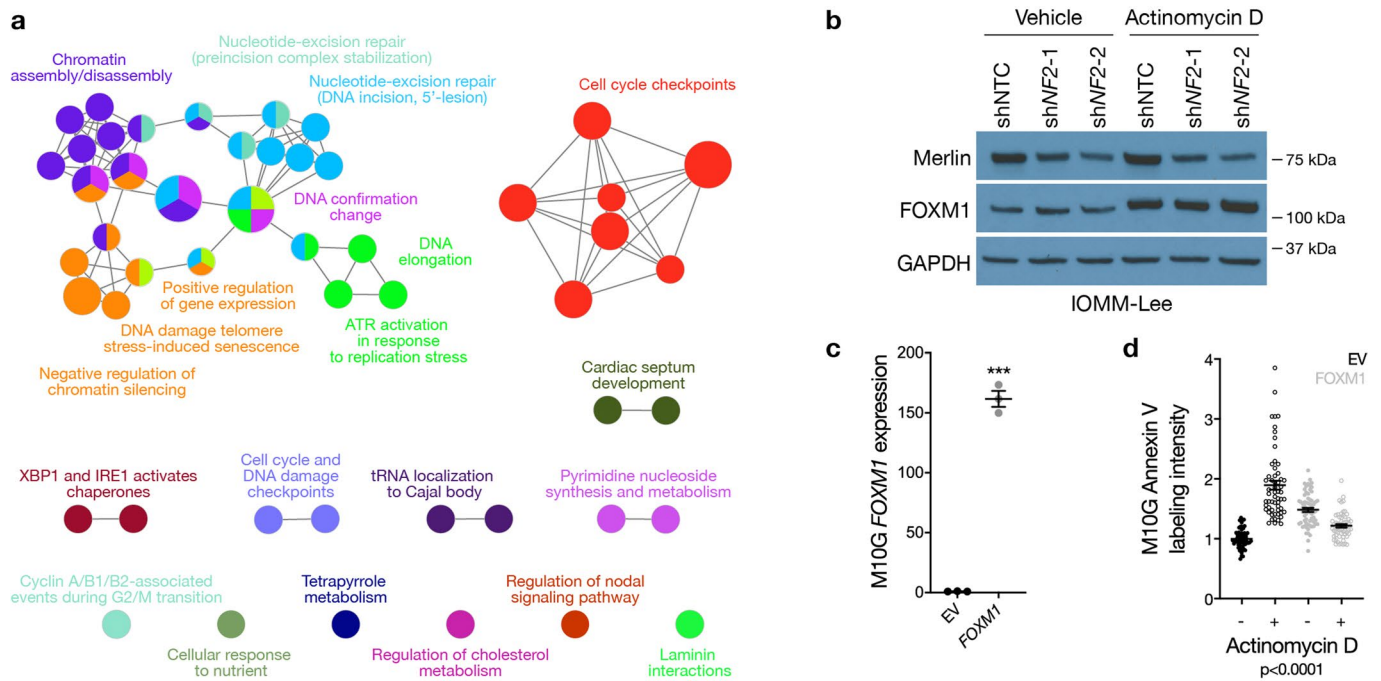
Extended Data Fig. 7 | FOXM1 target gene functions in meningiomas and meningioma cells. a, Predicted network of FOXM1-regulated pathways in Hypermitotic meningiomas based on H3K27ac ChIP sequencing of 25 meningiomas with matched RNA sequencing and DNA methylation profiling (15 Hypermitotic, 10 non-Hypermitotic). **b,** Immunoblot for Merlin, FOXM1, or GAPDH in IOMM-Lee meningioma cells stably expressing a non-targeting ontrol shRNA (shNTC) or shRNAs suppressing *NF2* (sh*NF2*-1 or sh*NF2*-2), after treatment with actinomycin D or vehicle control for 24 h. **c,** QPCR for *FOXM1* in M10G meningioma cells over-expressing FOXM1 or empty vector (EV). 3 biological replicates per condition. ***p≤0.0001 (Student's t test, one sided). **d,** Quantification of Annexin V confocal microscopy in M10G cells over-expressing FOXM1 or EV after treatment with actinomycin D or vehicle control for 24 h. From left to right, 57, 58, 65, or 60 cells are shown (ANOVA, one sided). Lines represent means, and error bars represent standard error of the means.
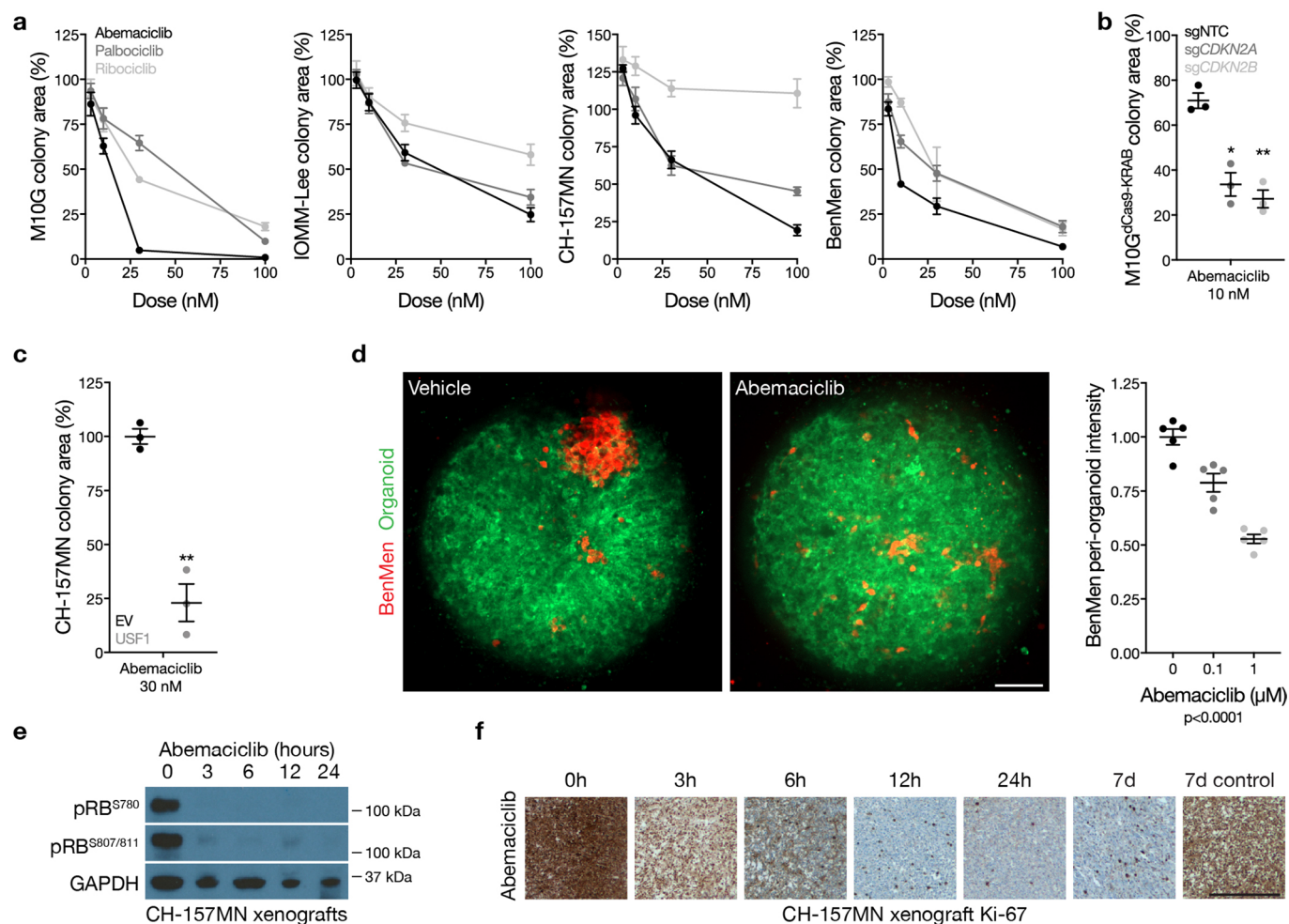
Extended Data Fig. 8 | Cell cycle inhibition blocks meningioma growth in cells, organoids, and xenografts. a, Relative colony area of M10G, BenMen, CH-157MN, or IOMM-Lee meningioma cells after 10 days of clonogenic growth and treatment with abemaciclib, ribociclib, or palbociclib. 3 biological replicates per condition per timepoint. **b**, Relative colony area of M10G$^{dCas9-KRAB}$ cells expressing sgNTC, sg*CDKN2A*, or sg*CDKN2B* after 10 days of clonogenic growth and treatment with abemaciclib. 3 biological replicates per condition. *p = 0.002, **p = 0.001 (Student's t test, one sided). Data are normalized to growth with vehicle treatment of each cell lines. **c**, Relative colony area of CH-157MN cells stably over-expressing USF or empty vector (EV) after 10 days of clonogenic growth and treatment with abemaciclib. 3 biological replicates per condition. **p = 0.001 (Student's t test, one sided). Data are normalized to growth with vehicle treatment of each cell lines. **d**, Quantification of BenMen peri-organoid intensity after 10 days of growth and treatment with abemaciclib or vehicle control Representative images of meningioma (red) and organoid (green) cells are shown. Scale bar 100 μM. 5 biological replicates per condition (ANOVA, one sided). **e**, Representative immunoblots from CH-157MN xenografts in NU/NU mice (left) harvested at intervals after a single treatment of abemaciclib (100 μg/g) via oral gavage (right). **f**, Representative images of CH-157MN xenograft Ki-67 immunohistochemistry after a daily treatment of abemaciclib or control. Scale bar 1mm. Lines represent means, and error bars represent standard error of the means.
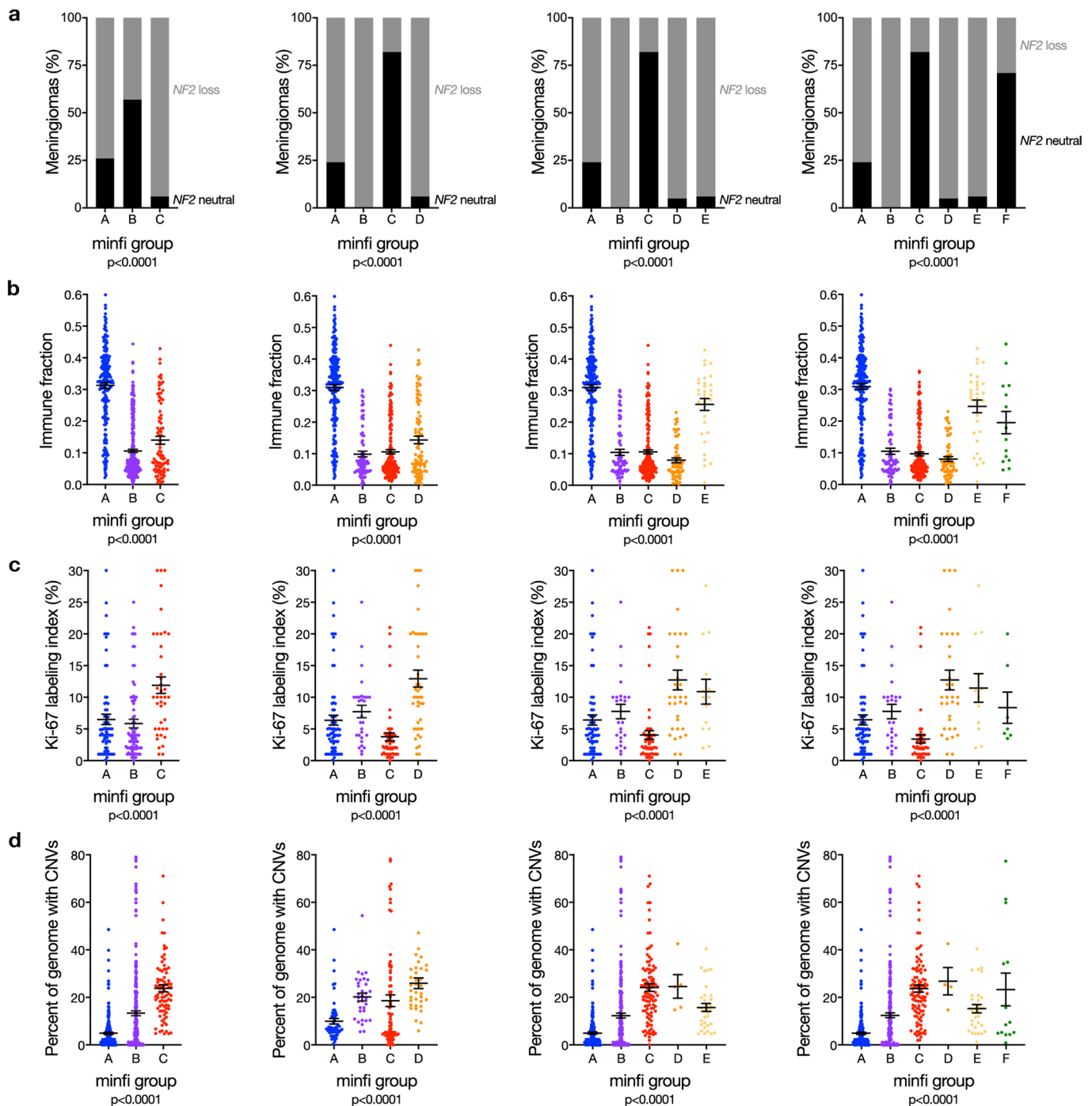
Extended Data Fig. 9 | Meningioma DNA methylation grouping schemes uncontrolled for the influence of CNVs on β values. a, Meningioma DNA methylation analysis of copy-number loss at the *NF2* locus (n = 565) across different numbers of DNA methylation groups determined by the minfi preprocessing pipeline (Chi-squared tests, two-sided). **b**, Meningioma DNA methylation estimation of leukocyte fraction (n = 565) across different numbers of DNA methylation groups determined by the minfi preprocessing pipeline (ANOVA, one sided). **c**, Ki-67 labeling index from meningioma clinical pathology reports (n = 206) across different numbers of DNA methylation groups determined by the minfi preprocessing pipeline (ANOVA, one sided). **d**, Meningioma genomes (n = 565) with copy-number variations (CNVs) across DNA methylation groups determined by the minfi preprocessing pipeline (ANOVA, one sided). Regardless of the number of groups, meningioma DNA methylation analysis uncontrolled for the influence of CNVs on β values cannot identify a grouping scheme with non-redundant differences in clinical outcomes (Extended Data Fig. 3d), *NF2* loss, immune enrichment, cell proliferation, and chromosome instability. Lines represent means, and error bars represent standard error of the means. minfi meningioma DNA methylation grouping schemed comprised of 3, 4, 5, or 6 groups are designated by letters A-C, A-D, A-E, or A-F, respectively.
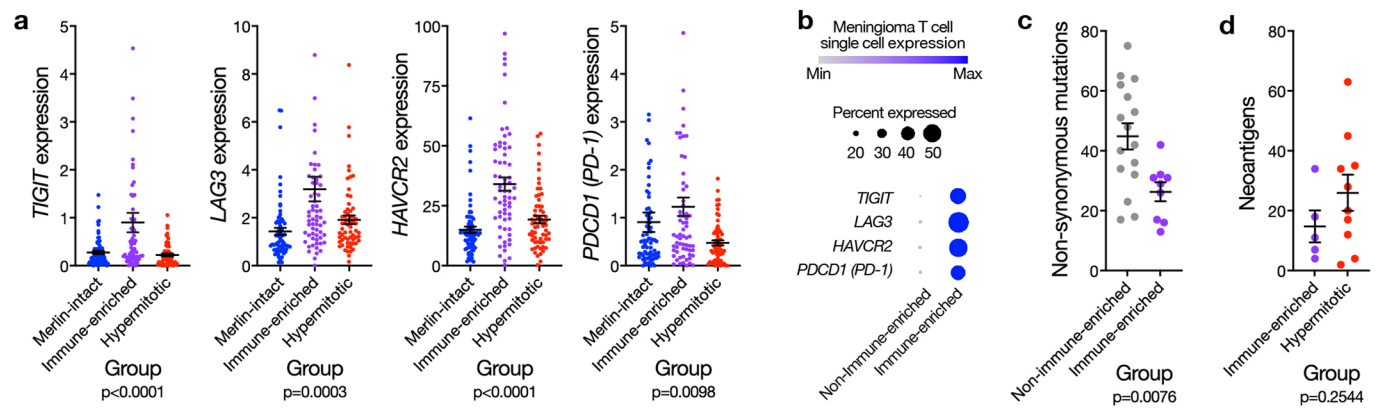
Extended Data Fig. 10 | Immune-enriched meningiomas display markers of T cell exhaustion and immunoediting. a, Meningioma transcripts per million (TPM) expression of *TIGIT*, *LAG3*, *HAVCR2*, or *PDCD1* (n = 200) T cell exhaustion markers across DNA methylation groups. Lines represent means, and error bars represent standard error of the means (ANOVA, one sided). **b**, Single-cell RNA sequencing relative expression of immune exhaustion genes in T cells across Immune-enriched (n = 5) and non-Immune-enriched (n = 3) meningioma samples. Circle size denotes percentage of cells. Circle shading denotes average expression. **c**, Non-synonymous mutations from whole-exome sequencing of Immune-enriched (n = 9) and non-Immune-enriched (n = 16) meningiomas, with paired normal samples, overlapping with the discovery cohort. Lines represent means, and error bars represent standard error of the means (Student's t test, one sided). **d**, Neoantigen prediction from whole-exome sequencing of Immune-enriched (n = 5) and Hypermitotic (n = 9) meningiomas, with paired normal samples, overlapping with the discovery cohort. Lines represent means, and error bars represent standard error of the means (Student's t test, one sided).

Corresponding author(s):   David R. Raleigh, MD, PhD

Last updated by author(s):   Mar 11, 2022

Reporting Summary

Nature Research wishes to improve the reproducibility of the work that we publish. This form provides structure for consistency and transparency in reporting. For further information on Nature Research policies, see our Editorial Policies and the Editorial Policy Checklist.

Statistics

For all statistical analyses, confirm that the following items are present in the figure legend, table legend, main text, or Methods section.

n/a	Confirmed	
☐	☒	The exact sample size (*n*) for each experimental group/condition, given as a discrete number and unit of measurement
☐	☒	A statement on whether measurements were taken from distinct samples or whether the same sample was measured repeatedly
☐	☒	The statistical test(s) used AND whether they are one- or two-sided *Only common tests should be described solely by name; describe more complex techniques in the Methods section.*
☐	☒	A description of all covariates tested
☐	☒	A description of any assumptions or corrections, such as tests of normality and adjustment for multiple comparisons
☐	☒	A full description of the statistical parameters including central tendency (e.g. means) or other basic estimates (e.g. regression coefficient) AND variation (e.g. standard deviation) or associated estimates of uncertainty (e.g. confidence intervals)
☐	☒	For null hypothesis testing, the test statistic (e.g. F, t, r) with confidence intervals, effect sizes, degrees of freedom and P value noted *Give P values as exact values whenever suitable.*
☒	☐	For Bayesian analysis, information on the choice of priors and Markov chain Monte Carlo settings
☐	☒	For hierarchical and complex designs, identification of the appropriate level for tests and full reporting of outcomes
☐	☒	Estimates of effect sizes (e.g. Cohen's *d*, Pearson's *r*), indicating how they were calculated

Our web collection on statistics for biologists contains articles on many of the points above.

Software and code

Policy information about availability of computer code

Data collection	No software was used for data collection.
Data analysis	The open-source software, tools, and packages used for data analysis in this study, as well as the version of each program, were ImageJ (v2.1.0), R (v3.5.3 and v3.6.1), FASTQC (v0.11.9), HISAT2 (v2.1.0), featureCounts (v2.0.1), Seurat R package (v3.0.1), Harmony R package (v0.1), caret R package (v6.0-90), Rtsne R package (v0.15), PAMES R package (v2.6.2), CONICSmat R package (v1.0), DeepTools (v3.1.2), survival R package (v3.2-13), survAUC R package (v1.0-5), rms R package (v6.2-0), rpart R package (v4.1.16), DynNom R package (v5.0.1), DESeq2 (Bioconductor v3.10), SeSAMe (Bioconductor v3.10), minfi (Bioconductor v3.10), karyoplotR (Bioconductor v3.10), ConsensusClusterPlus (Bioconductor v3.10), and DiffBind (Bioconductor v3.10). No software was used for data collection. A methylation profile multi-class support vector machine (SVM) classifier was generated using the caret R package, and was deposited in the github repository abrarc/meningioma-svm (DOI:10.5281/enodo.6353877). In brief, a linear kernel SVM was constructed using training data comprising 75% of randomly selected samples from the discovery cohort (n=150) with 10-fold cross validation. 2,000 probes from each pre-processing pipeline were used as variables. The remaining 25% of samples from the discover cohort (n=50) were used to test the model, which performed with 97.9% accuracy when classifying samples into 3 SeSAMe groups (95% CI 89.2-99.9%, p<2.2x10-16). SVM classifiers for 3, 4, 5, or 6 minfi groups were generated using the same approach and performed with 91.8% (95% CI 80.4%-97.7%, p=4.69x10-9), 91.8% (95% CI 80.4%-97.7%, p=9.58x10-16), 93.8% (95% CI 82.8%-98.7%, p=2.98x10-16), and 93.6% (95% CI 82.5%-98.7%, p<2.2x10-16) accuracy, respectively. SVM classification and K-means consensus clustering of the validation cohort was performed with the same parameters as for the discovery cohort using the same probes in the validation cohort that were identified from the discovery cohort.

For manuscripts utilizing custom algorithms or software that are central to the research but not yet described in published literature, software must be made available to editors and reviewers. We strongly encourage code deposition in a community repository (e.g. GitHub). See the Nature Research guidelines for submitting code & software for further information.

Data

All manuscripts must include a data availability statement. This statement should provide the following information, where applicable:

- Accession codes, unique identifiers, or web links for publicly available datasets
- A list of figures that have associated raw data
- A description of any restrictions on data availability

DNA methylation (n=565), RNA sequencing (n=185), and single-cell RNA sequencing data (n=8 meningioma samples, n=2 dura samples) of new samples reported in this manuscript have been deposited in the NCBI Gene Expression Omnibus under the accession GSE183656 (https://www.ncbi.nlm.nih.gov/geo/query/acc.cgi?acc=GSE183656). Additional RNA sequencing data from previously reported meningiomas (n=15) from the discovery cohort are available under the accession GSE101638 (https://www.ncbi.nlm.nih.gov/geo/query/acc.cgi?acc=GSE101638). Whole exome sequencing, ChIP sequencing, and additional DNA methylation profiling data incorporated into this study were derived from previously reported and deposited meningiomas in GSE101638 (https://www.ncbi.nlm.nih.gov/geo/query/acc.cgi?acc=GSE101638), GSE139652 (https://www.ncbi.xyz/geo/query/acc.cgi?acc=GSE139652), and . The publicly available GRCh38 (hg38, https://www.ncbi.nlm.nih.gov/assembly/GCF_000001405.39/) and CRCh37.p13 datasets (hg19, https://www.ncbi.nlm.nih.gov/assembly/GCF_000001405.25/) were used in this study.

Field-specific reporting

Please select the one below that is the best fit for your research. If you are not sure, read the appropriate sections before making your selection.

☒ Life sciences   ☐ Behavioural & social sciences   ☐ Ecological, evolutionary & environmental sciences

For a reference copy of the document with all sections, see nature.com/documents/nr-reporting-summary-flat.pdf

Life sciences study design

All studies must disclose on these points even when the disclosure is negative.

Sample size	No statistical methods were used to predetermine clinical sample sizes, but our discovery and validation cohort sizes are similar or larger to those reported in previous publications. All experiments were performed with independent biological replicates (2-3 biological replicates for molecular or cell biology experiments, and 7+ biological replicates for animal experiments). In our experience and in the experience from previous publications, these samples sizes provide sufficient resolution to resolve biologically-meaningful differences between conditions tested using molecular, cellular, or animal techniques. To validate this approach, all experiments were repeated, and statistics were derived from biological replicates (rather than technical replicates). Biological replicates are indicated in each panel or figure legend. Data distribution was assumed to be normal, but this was not formally tested.
Data exclusions	No clinical, molecular, cellular, or animal data points were excluded from the analyses.
Replication	All experiments were performed with at least 3 biologic replicates. All attempts at replication were successful.
Randomization	This was a retrospective non-randomized study of human tumor samples with no intervention. All samples were interrogated equally. Thus, controlling for covariants among clinical samples is not relevant. Cells, organoids, and animals were randomized across experimental conditions, but pre-treatment tumor sizes and other potentially-confounding covariates were controlled across conditions before experimentation.
Blinding	Investigators were blinded to conditions during clinical data collection and analysis of mechanistic or functional studies. Bioinformatic analyses were performed blind to clinical features, outcomes, or molecular characteristics.

Reporting for specific materials, systems and methods

We require information from authors about some types of materials, experimental systems and methods used in many studies. Here, indicate whether each material, system or method listed is relevant to your study. If you are not sure if a list item applies to your research, read the appropriate section before selecting a response.

Materials & experimental systems

n/a	Involved in the study
☐	☒ Antibodies
☐	☒ Eukaryotic cell lines
☒	☐ Palaeontology and archaeology
☐	☒ Animals and other organisms
☐	☒ Human research participants
☒	☐ Clinical data
☒	☐ Dual use research of concern

Methods

n/a	Involved in the study
☒	☐ ChIP-seq
☒	☐ Flow cytometry
☒	☐ MRI-based neuroimaging

Antibodies

Antibodies used	-Merlin (#ab88957, clone AF1G4, Abcam, 1:2000) -GAPDH (#MA515738, clone GA1R, Thermo Fischer Scientific, 1:2000) -Caspase-7 (#9492, Cell Signaling, 1:500) -IRF8 (#5628S, clone D20D8, Cell Signaling, 1:500) -Tubulin (#T5168, clone B-5-1-2, Sigma, 1:5000) -HH3 (#702023, clone 17H2L9, Thermo Fischer Scientific, 1:1000) -FLAG (#F1804, clone F1804, Sigma, 1:1000) -ARHGAP35 (#2860, clone C59F7, Cell Signaling, 1:1000) -FOXM1 (#sc-376471, clone G-5, Santa Cruz, 1:500) -pRB-S780 (#8180P, clone D59B7, Cell Signaling, 1:1000) -pRB-S807/811 (#8516P, clone D20B12, Cell Signaling, 1:1000) -Anti-mouse HRP-conjugated secondary antibody (#7076, Cell Signaling, 1:2000) -Anti-rabbit HRP-conjugated secondary antibody (#7074, Cell Signaling, 1:2000) -LYVE-1 (#ab14917, Abcam, 1:1000) -PROX-1 (#AF2727, R&D Systems, 1:1000) -Anti-rabbit Alexa Fluor secondary antibody (#A21206, Thermo Fischer Scientific, 1:1000) -Anti-goat Alexa Fluor secondary antibody (#A21469, Thermo Fischer Scientific 1:1000) -FOXM1 (#ab207298, clone EPR17379, Abcam, 1:600) -Ki-67 (#790-4286, clone 30-9, Ventana, 1:6) -cleaved Caspase-3 (#9664, clone 5A1E, Cell Signaling, 1:2000) -CD3 (#A0452, Agilent Technologies, 1:200)
Validation	-Merlin: Knockout validated for human immunoblots. -GAPDH: Knockout validated for human immunoblots. -Caspase-7: Validated +/- apoptosis induction for human immunoblots. -IRF8: Validated +/- IFN stimulation for human immunoblots. An unknown background band is detected at 80 kDa in some cell lines. -Tubulin: Validated for human immunoblots using recombinant expressed antibodies, genetic strategies, independent antibody verification, RNA sequencing, functional assays, expression/overexpression, and immunocapture followed by mass spectrometry. -HH3: Validated for human immunoblots using subcellular fractionation. -FLAG: Validated for human immunoblots and immunoprecipitation using affinity purification and competition assays. -ARHGAP35: Validated for human immunoblots using immunoprecipitation -FOXM1: Validated for human immunoblots using overexpression -pRB-S780: Validated for human immunoblots using phosphorylated or nonphosphorylated recombinant truncated Rb with or without RB blocking peptides. -pRB-S807/811 : Validated for human immunoblots using phosphorylated or nonphosphorylated recombinant truncated Rb with or without RB blocking peptides. -Anti-mouse HRP-conjugated secondary antibody: Validated for human immunoblots using affinity purification and competition assays. -Anti-rabbit HRP-conjugated secondary antibody: Validated for human immunoblots using affinity purification and competition assays. -LYVE-1: Knockout validated for human imunofluorescence. -PROX-1: Validated for human immunofluorescence using subcellular localization. -Anti-rabbit Alexa Fluor secondary antibody: Validated for human immunofluorescence using affinity purification. -Anti-goat Alexa Fluor secondary antibody: Validated for human immunofluorescence using affinity purification. -FOXM1: Validated for human immunofluorescence using recombinant expressed antibodies. -Ki-67: Validated for human immunohistochemistry and immunofluorescence using proliferating versus non-proliferating tissues. -cleaved Caspase-3: Validated +/- apoptosis induction for human immunohistochemistry -CD3: Validated for human immunohistochemistry using T-cell versus B-cell lines.

Eukaryotic cell lines

Policy information about cell lines

Cell line source(s)	HEK293T cells were obtained from ATCC. CH-157MN, IOMM-Lee, DI-98, DI-134, MSC1, and M10G primary meningioma cell lines were obtained from collaborators or derived from patient tumor samples and described in previous studies, as referenced in the Methods section.
Authentication	Meningioma cell lines were authenticated using DNA methylation profiling and CNV analyses to confirm concordance to tumors of origin, most recently in 2021. Non-meningioma cell lines purchased from reputable commercial suppliers (HEK293T cells from ATCC) were not authenticated.
Mycoplasma contamination	All cell lines tested negative for mycoplasma.
Commonly misidentified lines (See ICLAC register)	No commonly misidentified cell lines were used in this study.

Animals and other organisms

Policy information about studies involving animals; ARRIVE guidelines recommended for reporting animal research

Laboratory animals	5-6 week old female NU/NU mice purchased from Harlan Sprague Dawley for this study. All animal care and experimental procedures were in accordance with federal policies and guidelines governing the use of animals and were approved by the University of California San Francisco's (UCSF) Institutional Animal Care and Use Committee (IACUC). The IACUC is in full compliance with the 8th edition of The Guide for the Care and use of Laboratory Animals. UCSF has an AAALAC accredited animal care and use program. Mice were housed in solid-bottomed cages containing autoclaved paper chips in individually ventilated cages. Animals had continuous access to irradiated food and water purified by reverse osmosis and UV lighting. The housing room was maintained at 68 to 74º Fahrenheit with 30-70 % relative humidity. All cages were maintained in a SPF barrier facility from which dirty bedding sentinel mice were tested quarterly. All sentinels were found to be seronegative for mouse hepatitis virus, pneumonia virus of mice, mouse parvovirus, minute virus of mice, epizootic diarrhea of infant mice, Theiler's murine encephalomyelitis virus, ectromelia and were free of ectoparasites and endoparasites. Mice were observed daily by animal care staff for any clinical abnormalities.
Wild animals	Study did not involve wild animals.
Field-collected samples	Study did not involve samples collected in the field.
Ethics oversight	Study was approved by the UCSF Institutional Animal Care and Use Committee (AN174769).

Note that full information on the approval of the study protocol must also be provided in the manuscript.

Human research participants

Policy information about studies involving human research participants

Population characteristics	Patients undergoing resection of meningioma at UCSF or HKU of all ages, genders, past and current diagnosis and treatment categories were included. Covariates are summarized in Supplementary table 1, and are recapitulated here:
	
	Patients: 565
	Median age: 58 years
	Median follow-up: 5.6 years
	Male:Female (ratio): 193:372 (1:1.93)
	Recurrences: 161
	Extent of resection
	    Gross total: 394 (70%)
	    Near total: 171 (30%)
	WHO grade
	    1 : 388 (69%)
	    2 (atypical): 142 (25%)
	    3 (anaplastic): 35 (6%)

Recruitment	As part of routine clinical practice at UCSF and HKU institutions, all patients undergoing craniotomy for tumor resection sign a waiver of informed consent to contribute de-identified data to research projects. Thus, there was no self-selection bias or other biases that may influence or impact our results. Meningioma samples for the discovery cohort were selected from the UCSF Brain Tumor Center Biorepository and Pathology Core in 2017, with an emphasis on high-grade meningiomas and low-grade meningiomas with long clinical follow-up. All WHO grade 2 and grade 3 meningiomas with available frozen samples were included. For WHO grade 1 meningiomas, frozen samples in the tissue bank were cross-referenced for clinical follow-up data from a retrospective institutional meningioma clinical outcomes database, and all cases with available frozen tissue and clinical follow-up greater than 10 years (n=40) were included. To achieve a discovery cohort of 200 cases, additional WHO grade 1 meningiomas with available frozen tissue and the longest possible clinical follow-up (albeit less than 10 years, n=47) were included. The electronic medical record was reviewed for all patients in late 2018, and paper charts were reviewed in early 2019 for patients treated prior to the advent of the electronic medical record. All available clinical pathology material was reviewed for diagnostic accuracy by a board-certified neuropathologist (D.A.S.). WHO grading was performed using contemporary criteria outlined in the WHO classification of tumors of the central nervous system. Cases for which other tumors remained in the differential diagnosis (such as schwannoma or solitary fibrous tumor/hemangiopericytoma) were excluded. The validation cohort was comprised of 365 consecutive meningiomas from patients who were treated at The University of Hong Kong (HKU) from 2000 to 2019 that had frozen tissue suitable for DNA methylation profiling. The medical record was reviewed for all patients in late 2019. For the discovery and validation cohorts, meningioma recurrence was defined as new radiographic tumor on magnetic resonance imaging after gross total resection, or enlargement/progression/growth of residual tumor on magnetic resonance imaging after subtotal resection. All magnetic resonance imaging studies in the discovery cohort were reviewed for accuracy and meningioma location by a board-certified radiologist with a Certificate of Added Qualification in Neuroradiology (J.E.V-M.) (Supplementary note). Nomograms integrating clinical and molecular features influencing meningioma outcomes were developed to guide clinical translation of meningioma DNA methylation groups (Supplementary note).
Ethics oversight	This study complied with all relevant ethical regulations and was approved by the UCSF Institutional Review Board (IRB #13-12587, #17-22324, #17-23196, and #18-24633), and by the HKU Institutional Review Board (UW 07-273 and UW 21-112). Meningiomas and de-identified clinical information were transferred from HKU to UCSF in 2019 for analysis under protection of a Material Transfer Agreement that was certified by both institutions.

Note that full information on the approval of the study protocol must also be provided in the manuscript.